

# On the dynamic response of adhesively bonded structures

M. Lißner<sup>a</sup>, E. Alabort<sup>a,b</sup>, B. Erice<sup>e</sup>, H. Cui<sup>c</sup>, B.R.K. Blackman<sup>d</sup>, N. Petrinic<sup>a</sup>

<sup>a</sup>Department of Engineering Science, University of Oxford, Parks Road, Oxford, OX1 3PJ, United Kingdom

<sup>b</sup>Oxmet Technologies Ltd., Unit 15, Oxford Industrial Park, Yarnton, OX5 1QU, United Kingdom

<sup>c</sup>School of Aerospace, Transport and Manufacturing, Cranfield University, Bedford, MK43 0AL, United Kingdom

<sup>d</sup>Department of Mechanical Engineering, Imperial College, London, SW7 2AZ, United Kingdom

<sup>e</sup>Department of Structural Engineering, NTNU, Trondheim, 7491, Norway

---

## Abstract

Fracture mechanics experiments are used to investigate the rate-dependent failure of adhesively bonded structures under different deformation modes: I, II and I/II. First, the high-rate mechanical response of the adhesive interface is analysed with a newly developed method – which relies entirely upon digital image correlation. The method was purposely designed to avoid any dynamic effects which may be present. This novel method is verified against quasi-static standard methods showing good agreement. Finally, simulations of the experiments are used to validate a cohesive zone model of the adhesive. The ability of the model to predict cohesive failure under a wide range of strain rates and deformation modes is demonstrated.

*Keywords:* adhesive joints, dynamic loading, cohesive zone modelling, experimental mechanics, impact behaviour

---

## 1. Introduction

Hybrid material combinations, such as composite-metal adhesive joints, are increasingly employed in several industries where energy efficiency improvements rely upon weight reduction whilst maintaining the structural integrity [1]. Understanding the failure performance for each material individually is key for establishing failure design and criteria for hybrid structures. The fracture energy  $J$ , and the failure strength are material parameters of paramount importance for the optimal design of these structures. Accurate experimentation is critical in the identification of the failure sequence of adhesively bonded structures. However, most of the experimental methods available in the literature lack accuracy – particularly when high strain rates and impact events are involved [2].

1 Several studies have investigated the failure strength of adhesive joints under quasi-static and  
2 dynamic loading conditions [3, 4, 5, 6, 7, 8, 9, 10, 11, 12, 13, 14]. In quasi-static loading conditions,  
3 typical butt joints [6, 9] and ring specimens [4] have been used to investigate the failure strength in  
4 the normal direction to the adhesive interface. For the shear loading behaviour, adhesive joints are  
5 commonly tested using the single lap joints (SLJ) [10] and double lap joints (DLS) [8]. Most dynamic  
6 investigations employ hydraulic testing machines or the Split Hopkinson Bar (SHB). The SHB is  
7 used extensively to measure the dynamic failure strength of adhesive joints [3, 5, 6, 9, 12, 13, 14].  
8 Other studies have employed the SHB with SLJ [15], pin-collar-specimens [3], torsion specimens  
9 [7] and cubic specimens [13, 14] to investigate the adhesive strength under shear deformation.  
10 Others have investigated the failure strength of the adhesive in normal direction to the adhesive  
11 interface using butt joints [6, 9], hat-shaped butt joints [5] and cubic joints [11, 12]. All these  
12 investigations obtained a strong dependence of the mechanical response of adhesive joints on the  
13 applied strain rate. Moreover, studies have encountered heat dissipation during the damage process  
14 of the adhesive joint in dynamic loading environments which is believed to be dependent on the  
15 strain rate [16, 12, 13]. Nevertheless, the strain and displacement measurements remain critical  
16 when analysing the strain and displacement based on the SHB analysis. It is believed that high-  
17 speed cameras in combination with digital image correlation (DIC) increases the accuracy of the  
18 relevant adhesive interfaces measurements [17].

19 Most methods for deriving the fracture energy were developed with quasi-static observations in  
20 mind. However, adhesively bonded structures are also subjected to dynamic loading. In those cases,  
21 one requires understanding of the performance of the adhesive in rate-dependent environments. Few  
22 investigations have focussed on understanding the fracture energy behaviour as a function of the  
23 loading rate [18, 19, 20, 21]. Isakov *et al.* used wedge DCB experiments (WDCB) to obtain the  
24 fracture energy by measuring the compliance [20]. Others have employed strain gauges attached  
25 to the beam to calculate the force over the bending strain [21], thus allowing the use of classical  
26 methods to obtain the fracture energy. For ENF experiments, researchers have measured the  
27 fracture energy by extracting the force from the strain gauge data and the displacement using  
28 high-speed cameras in the Split Hopkinson bar [18, 19]. However, signal filtering is required in  
29 order to obtain a suitable force-displacement response to derive the fracture energy. Moreover, the  
30 calculation of the fracture energy under dynamic loading employing the aforementioned techniques  
31 needs careful consideration. Dynamic effects such as inertia and oscillation of the beams should be

1 considered – if those are not negligible, the measurements may lack accuracy.

2 With the above in mind, this paper presents a new method to identify the mechanical per-  
3 formance of the adhesive interface dependent on rate and mode of fracture. Firstly, quasi-static  
4 and high-rate experiments for three different fracture modes: mode I, mode II and mixed-mode  
5 I/II are carried out using the WDCB, ENF and SLB test specimens respectively. Secondly, a new  
6 measurement technique is employed to derive the high-rate force-displacement curves. Thirdly, the  
7 quasi-static measurements are compared to traditional analyses, thus validating the new approach.  
8 Finally, the quasi-static and high-rate experiments are simulated using a finite element methods.  
9 The models employ a cohesive zone model developed previously by the authors [15]. Experimental  
10 results are used to validate the cohesive zone model and to compare; (i) the ability of the model to  
11 predict failure; and (ii) the validity of the developed experimental technique to measure adhesively  
12 bonded structures under different rate- and mode-dependent environments.

## 13 **2. Background**

14 Many researchers have investigated different ways to measure the fracture energy of adhesive  
15 interfaces using fracture mechanics experiments under different fracture modes [22, 23, 24, 25, 26].  
16 The double cantilever beam (DCB) is generally used to investigate the mechanical performance of  
17 the adhesive interface normal to its surface [22, 23, 26, 27, 28, 29, 30], while the end notched flexure  
18 (ENF) resolves the adhesive’s response tangential to its surface [24, 26, 31, 32, 33]. The single  
19 leg beam (SLB) is usually employed to reveal the adhesive’s mechanical performance under more  
20 complex stress states [25, 26]. The DCB is believed to be of more relevant practical importance, but  
21 in practice, a pure fracture mode does not exist. All of these methods have one thing in common:  
22 one needs to measure the crack length during the failure process to calculate the fracture energy by  
23 means of beam theory. For this, several approaches have been developed: (i) measuring the crack  
24 length directly by crack length monitoring [22, 27, 34, 35, 36] or (ii) estimating the crack length by  
25 measurement of the compliance [33, 37, 38, 39]. However, the calculation of the fracture energy is  
26 challenging when relying upon monitoring of the crack length.

27 Unfortunately, a few studies [40, 41, 42, 43] have experienced unstable crack propagation which  
28 prevents a clear observation of the crack tip. Moreover, clear visibility of the crack is difficult  
29 for certain adhesives. This can have a non-negligible effect on the compliance derived from the  
30 crack length in the classic compliance calibrated method (CCM) [44]. Also, when using ductile

1 adhesive systems, the energy dissipated at the fracture process zone (FPZ) can be large [32] –  
 2 this can influence the accuracy of the results. The calculation of the fracture energy – based on  
 3 beam theory – is underestimated when the aforementioned effects are ignored. Thus, improved  
 4 approaches have been developed to correct the calculation, for example by the use of direct beam  
 5 theory (DBT) [45] or corrected beam theory (CBT) [46]. However, those methods also rely upon  
 6 the accurate measurement of the crack length – this is challenging, even more so at high strain rates.  
 7 De Moura *et al.* introduced the compliance based beam method (CBBM) [33] to avoid the need  
 8 to measure the actual crack length propagation. This approach relies entirely upon the compliance  
 9 performance during the failure process. This method considers the FPZ which is formed due to  
 10 multiple micro-crack nucleations within the adhesive thickness and plastification of the adhesive.  
 11 Using this approach, the dissipated energy in the FPZ of ductile adhesives is considered in the final  
 12 result of the fracture energy. Other researchers based their crack length measurement on digital  
 13 image correlation (DIC) recordings to avoid the difficult crack length monitoring [47, 48].

14 For the calculation of the force-displacement responses of WDCB, ENF and SLB specimens the  
 15 CBBM is considered to account for the FPZ. Using the CBBM approach, a direct measurement  
 16 of the crack length is not required. Based on simple beam theory and Timoshenko beam theory,  
 17 the mathematical relationships necessary for calculating the crack length can be derived. Therefore  
 18 one only needs to monitor the applied load and displacement during the experiment. The follow-  
 19 ing equations are used for our analysis method and are presented and summarised here for the  
 20 reader’s convenience. Figure 1(a) provides an overview of the orientation and nomenclature used  
 21 for generating the mathematical relationships for each specimen configuration.

22 Based on simple beam theory (SBT) and considering Timoshenko beam theory – to account for  
 23 shear effects – the strain energy  $\Pi$  for the WDCB experiments can be deduced from

$$\Pi = 2 \left[ \int_0^a \frac{M^2}{2EI} dx + \int_0^a \int_{-\frac{h}{2}}^{\frac{h}{2}} \frac{\tau^2}{2G} b dz dx \right] \quad (1)$$

24 where  $M$  is the bending moment,  $h$  is the thickness,  $E$  is the Young’s modulus,  $G$  is the shear  
 25 modulus of the adherent,  $I$  is the second moment of inertia, and  $\tau$  is the shear stress which is  
 26 determined following

$$\tau = \frac{3}{2} \frac{V}{bh} \left( 1 - \frac{y^2}{c^2} \right) \quad (2)$$



1 where  $V$  is the shear force, and  $c = h/2$ . Using the Castelgiano theorem following

$$u = \frac{d\Pi}{dF} \quad (3)$$

2 where  $u$  is the displacement, and  $F$  is the vertical force, the WDCB compliance can be calculated  
3 employing

$$F(u) = \frac{u}{C} \quad (4)$$

4 and

$$C(a) = \frac{8a^3}{Eb^3h^3} + \frac{12a}{5bhG} \quad (5)$$

5 where  $G$  is the shear modulus of the adherent. For the ENF and SLB specimens, the strain  
6 energy  $\Pi$  can be written as

$$\Pi = \int_0^{2L} \frac{M^2}{2EI} dx + \int_0^{2L} \int_{-h}^h \frac{\tau^2}{2G} b dz dx. \quad (6)$$

7 Thus, the compliance  $C$  for the ENF [33] and SLB [25] experiments can be obtained using

$$C(a) = \frac{3a^3 + 2L^3}{8bh^3E} + \frac{3L}{10bhG} \quad (7)$$

8 and

$$C(a) = \frac{28a^3 + L^3}{32Eb^3h^3} + \frac{3(a + L)}{20Gbh} \quad (8)$$

9 respectively, where  $E$  is the Young's modulus,  $b$  the specimen width,  $h$  the thickness of the  
10 adherent,  $G$  the shear modulus,  $a$  the crack length and  $L$  the characteristic specimen length.

11 Finally, the applied force is determined using Eq.4 and considering that  $C$  involves the total  
12 compliance of both adherents. The force, displacement and crack length results can then be utilised  
13 to generate the fracture energy for each fracture mode. Although, the intention of this paper is to  
14 provide force-displacement data sets for quasi-static and high-rate loading regimes in order to prove  
15 the validity of a cohesive zone model developed, the equations for the fracture energy are provided  
16 for further comparison. The fracture energy for the WDCB experiments,  $J_{Ic}$ , can be calculated

1 using [49]

$$J_{Ic}(a, F) = \frac{12a^2}{Eh^3b^2}F^2 + \frac{F}{b}(w'_1 - w'_2) \quad (9)$$

2 where  $w'_1$  and  $w'_2$  are the beam rotations.

The fracture energy,  $J_{IIc}$ , for the ENF specimens was obtained using the approach of the equivalent crack length  $a_e$  [33]. The quasi-static measurements  $a_e$  is calculated as

$$a_e = \left[ \frac{C_c}{C_{0c}}a_0^3 + \frac{2}{3} \left( \frac{C_c}{C_{0c}} - 1 \right) L^3 \right]^{\frac{1}{3}} \quad (10)$$

3 with

$$C_c = C - \frac{3L}{10bhG} \quad \text{and} \quad C_{0c} = C_0 - \frac{3L}{10bhG} \quad . \quad (11)$$

4 The fracture energy can then be fully described using the flexural modulus  $E_f$ .  $E_f$  is calculated  
5 following

$$E_f = \frac{3a_0^3 + 2L^3}{8bh^3} \left( C_0 - \frac{3L}{10bhG} \right)^{-1} \quad (12)$$

6 The flexure modulus can then be employed to calculate the fracture energy following

$$J_{IIc}(a_e, F) = \frac{9F^2a_e^2}{16b^2h^3E_f} \quad (13)$$

7 Accordingly, the fracture energy for the SLB configuration,  $J_{I/IIc}$ , can be calculated using

$$J_{I/IIc}(a, F) = \frac{21F^2a^2}{16E_fb^2h^3} + \frac{3F^2}{10Gb^2h} \quad (14)$$

8 while the normal and tangential components are described following

$$J_{Ic}(a, F) = \frac{12F^2a^2}{16E_fb^2h^3} + \frac{3F^2}{10Gb^2h} \quad (15)$$

9 and

$$J_{IIc}(a, F) = \frac{9F^2a^2}{16E_fb^2h^3} \quad (16)$$

1        respectively. The SLB fracture energy is then fully defined for the quasi-static loading case using  
2 Equations 4 and 8.

### 3 **3. Experimental methods**

#### 4 *3.1. Adherent and adhesive materials*

5        The thermosetting epoxy film adhesive AF 163-2OST from Scotch-Weld<sup>TM</sup> was used to bond  
6 two titanium alloy Ti-6Al-4V adherents. The film adhesive is supported with a glass fibre carrier  
7 mat which enables improved handling for large scale applications. Different sample geometries were  
8 designed and manufactured to measure fracture properties under three different loading modes: The  
9 wedge double cantilever beam (WDCB) specimen was used to study the mechanical performance of  
10 the adhesive interface when loaded normal to the adhesive surface (mode I). The shear behaviour  
11 (mode II) was experimentally studied with the end notched flexure (ENF) specimen, while a com-  
12 bination of both modes (I/II) was investigated using the single leg beam (SLB) specimen. The  
13 optimum specimen dimensions have been determined to ensure the specimens ability to reveal the  
14 mechanical performance of the adhesive interface under Split Hopkinson Bar loading without in-  
15 terference in the form of plastic deformation of the adherents. Hence, the beam length is  $L = 146$   
16 mm, the width is  $b = 20$  mm and the height is  $h = 4$ mm. Considering the relationship [50]

$$a_{0,cr} = 0.35 \cdot L \quad (17)$$

17        the critical initial crack length for stable crack propagation is  $a_{0,cr} = 23.8$  mm. Therefore, the  
18 initial crack length for the WDCB specimens are defined as  $a_0 = 30$  mm, while for ENF and SLB  
19 specimens it is  $a_0 = 34$  mm. The dimensions for each specimen configuration are shown in Figure  
20 1(b).

#### 21 *3.2. Specimen manufacturing and preparation*

22        Figure 2(a) shows a custom made bonding fixture which was designed to accurately manufacture  
23 the specimens. Spacers were used to obtain the desired interface thickness. Bonding requires  
24 the activation of the adherent's surface to obtain optimal properties. Thus, the to-be-bonded  
25 surfaces were grit-blasted, cleaned and anodised following the procedure described elsewhere [51].  
26 To introduce the crack length, a  $12.0 \mu\text{m}$  thick Teflon sheet was introduced between two layers of

1 film adhesive. The measured interface thickness of the manufactured specimens is reported for each  
2 fracture mode in Figure 2(b). A deviation of 2.3 %, 2.3 % and 1.6 % for the WDCB , ENF and  
3 SLB specimens from the nominal adhesive thickness of  $t_a = 0.25$  mm was observed.

### 4 3.3. Experimental setup

5 The quasi-static (QS) and high-rate (HR) experiments were performed in laboratory conditions.  
6 A screw-driven Zwick machine was employed to load the specimens quasi-statically with a constant  
7 cross-head velocity of  $v = 1$  mm/min. The load-displacement ( $F - u$ ) curve was recorded during the  
8 experiment. A standard camera recorded images of the tested specimen at a speed of two frames  
9 per second at a resolution of 1546 x 2152 pixels. A fine gray-scale speckle pattern was applied to  
10 the surface of the specimen to monitor the crack length using digital image correlation (DIC). The  
11 initial crack length was marked with a ruler as it is shown in Figure 3. The HR experiments were  
12 carried out using a Split Hopkinson Pressure Bar (SHPB) to subject the specimen to a velocity  
13 of  $v = 4$  m/s. The SHPB setup for WDCB, ENF and SLB are different. While the setup for the  
14 WDCB specimens consists traditionally of an input and output bar and a striker, the output bar  
15 in the setup for ENF and SLB specimens is replaced with an in-house-made fixture holding the  
16 specimen in place – see Figure 3. The diameter of the input and output bars is  $d = 16$ mm, while  
17 the length of the bars was  $L_b = 2500$  mm. The striker had a length of  $L_s = 2700$  mm with the  
18 same diameter as the input and output bars. Figure 4 shows the dimensions and the setup of the  
19 used SHPB. Images were recorded using two high-speed cameras: a Photron camera recorded the  
20 displacement of the loading wedge/ pin with 150,000 frames per second and a resolution of 716 x  
21 624 pixels, while a Special imaging Kirana camera monitored the crack length growth at 200,000  
22 frames per second with a resolution 924 x 768 pixels.

23 For both loading regimes, the supports and loading pin for the ENF and SLB experiments  
24 are manufactured with a rounded tip and a radius of  $r = 2.5$  mm. The wedge for the WDCB  
25 experiments is designed so that a sharp tip with an angle of  $\alpha = 30^\circ$  is achieved. The bars and  
26 striker were made out of titanium alloy Ti-6Al-4V while the supports were made out of stainless  
27 steel. Table 1 summarises the mechanical properties for the two alloys. Figure 3 summarises the  
28 difference in the setup for each specimen configuration.

29 One should note that in the present work, the SHPB is used exclusively to apply the dynamic  
30 deformation load at the fracture mechanics experiments – SHPB analysis theory was not employed.

Table 1: Material properties of adherents, bars, striker and supports.

Metal	$E$ (GPa)	$\rho$ (g/cm <sup>3</sup> )	$\nu$	$\sigma_y$ (MPa)
Ti-6Al-4V	114	4.43	0.34	900
Steel	200	8	0.29	-

1 Due to the large scale of the experiments – which introduce geometric and material impedance  
 2 mismatch, or inhomogeneous stress distribution – the authors believe that the readings from the  
 3 strain gauges will not offer the most accurate representation of the mechanical behaviour. Therefore,  
 4 a new data acquisition method has been developed which relies entirely on digital image correlation.  
 5 This new method is explained in the following sub-section.

#### 6 3.4. Data acquisition method

7 For calculating the fracture energy, one needs to measure the force and the crack length propa-  
 8 gation during the failure process. Generally, the force-displacement curves obtained using standard  
 9 equipment – *i.e.* testing machine output and DIC – are sufficient to obtain the  $J$  value. The CBBM  
 10 method can be applied to the quasi-static ENF and SLB experiment data. However, the quasi-static  
 11 force recordings of the WDCB specimens are influenced by the friction between the wedge and the  
 12 adherents: a transformation of the force in its perpendicular components – the actual opening force  
 13 – would need to consider those frictional effects. This introduces some uncertainties that would  
 14 influence the accuracy of the results. Additionally, high-rate force readings obtained from strain  
 15 gauge signals may not be accurate due to oscillations and inertia effects encountered during loading.  
 16 The measured forces would require smoothing and filtering – this may masks the true mechanical  
 17 performance of the joint. To overcome these limitations, a new measurement technique was devel-  
 18 oped. This technique overcomes the aforementioned challenges by exclusively relying upon digital  
 19 image correlation (DIC). Figure 5 illustrates the newly developed measurement technique. The  
 20 method is described in the following paragraph.

21 The force  $F$  was calculated using the applied displacement  $u$  and the compliance  $C$  of the  
 22 adherents using Eq.4. The calculation of the compliance requires the crack length  $a$  – or a sufficiently  
 23 high-resolution image. Therefore, this novel method relies upon measuring the applied displacement  
 24 and the crack length using DIC. Firstly, a measurement position, which is represented as a red dot  
 25 in Figure 5, is selected. Using this, the displacement is obtained as a function of the time. Secondly,

1 the crack length is estimated. A region of interest (ROI) is defined which includes the initial crack  
 2 length. These are shown as black lines in Figure 5. Thirdly, the stored displacement histories are  
 3 then used to indicate the crack length propagation for each time step. For that, two points in the  
 4 x-direction (which is aligned to the specimen width) are employed. These points are positioned on  
 5 each substrate close to the adhesive interface. The sets of points act as virtual gauges which are  
 6 used to obtain the opening displacement in the x-direction  $\Delta u$  (for WDCB) and in the y-direction  
 7  $\Delta v$  (for ENF and SLB) for each point-position. For ductile materials, a threshold is required to  
 8 define the opening displacement in order to consider the influence of the FPZ. This can be obtained  
 9 by measuring the opening displacement of the first crack propagation increment which is visible  
 10 using the displacement field in the image analysis. The following relationship is defined to identify  
 11 when displacements are larger than the threshold at the  $n^{th}$  position:

$$\Delta u_{(y=y_n)(t=t_s)} \geq \Delta u_{Threshold} \quad \text{and} \quad \Delta v_{(y=y_n)(t=t_s)} \geq \Delta v_{Threshold}. \quad (18)$$

12 When the threshold is reached, the distance of  $y_n$  can be used to derive the crack length  $a$  at  
 13 time  $t_s$  following

$$a_{t=t_s} = a_0 + y_{n(t=t_s)} \quad . \quad (19)$$

14 By deriving the crack length as a function of time, the compliance of the joint can be calculated.  
 15 Table 2 summarises the employed equations and measurement techniques for each loading regime  
 16 separately. Using the new data acquisition method to obtain the compliance, the applied force is  
 17 then calculated considering Eq.4. Thus, the force-displacement behaviour and the fracture energy-  
 18 crack length relationship are fully described.

Table 2: Overview of the employed equations for the calculation of the fracture energy in QS and HR loading regimes.

Equations for analysis	Wedge double cantilever beam (WDCB)	End notched flexure (ENF)	Single leg beam (SLB)
<b>Compliance</b>	$C(a) = \frac{8a^3}{Eb^3} + \frac{12a}{5bhG}$	$C(a) = \frac{3a^3+2L^3}{8bh^3E} + \frac{3L}{10bhG}$ $C_c = C - \frac{3L}{10bhG}$ and $C_{0c} = C_0 - \frac{3L}{10bhG}$	$C = \frac{F}{u}$
<b>Energy release rate</b>	$J_{Ic}(a, F) = \frac{12a^2}{Eh^3b^2} F^2 + \frac{F}{b} (w_1' - w_2')$ $w_1' - w_2'$ have been calculated following the procedure described in [49]	$J_{Ic}(a_e, F) = \frac{9F^2 a_e}{16b^2 h^3 E_f}$ with $E_f = \frac{3a_0^3+2L^3}{8bh^3} (C_0 - \frac{3L}{10bhG})^{-1}$	$J_{I/IIc}(a, F) = \frac{21F^2 a^2}{16E_f b^2 h^3} + \frac{3F^2}{10Gb^2 h}$ $J_{Ic}(a, F) = \frac{12F^2 a^2}{16E_f b^2 h^3} + \frac{3F^2}{10Gb^2 h}$ $J_{IIc}(a, F) = \frac{9F^2 a^2}{16E_f b^2 h^3}$ with $E_f = \frac{28a_0^3+L^3}{32bh^3} (C_0 - \frac{3(a_0+L)}{20bhG})^{-1}$
<b>Quasi-static</b>			
<b>Crack length</b>	Obtained with new measuring technique based on DIC using high-speed SI Kirana camera images	$a_e = \left[ \frac{C_c}{C_{0c}} a_0^3 + \frac{2}{3} \left( \frac{C_c}{C_{0c}} - 1 \right) L^3 \right]^{\frac{1}{3}}$	Transform cubic equation to obtain the crack length $a$
<b>Displacement</b>		DIC or testing machine output	$C(a) = \frac{28a^3+L^3}{32Eb^2h^3} + \frac{3(a+L)}{20Gb^2h}$
<b>Force</b>	$F(u) = \frac{u}{C}$	Testing machine output	
<b>High-rate</b>			
<b>Crack length</b>	Obtained with new measuring technique based on DIC using high-speed SI Kirana camera images		
<b>Displacement</b>	Obtained with DIC using high-speed Photron camera images		
<b>Force</b>		$F(u) = \frac{u}{C}$	

## 1 4. Experimental results

2 This section quantifies and discusses the rate- and mode-dependent behaviour of adhesively  
3 bonded structures. First, the new experimental methodology is verified by comparing different  
4 measurement techniques. Second, the mechanical behaviour – as measured by the novel experimen-  
5 tation – of the adhesively bonded structures is presented. Third, fractography is used to isolate the  
6 nature of the fracture mode.

### 7 4.1. Verification of the new data acquisition method

8 Before the new measurement technique can be applied, it is necessary to verify its accuracy. This  
9 will add confidence to the obtained results. For this purpose, a verification process is proposed in  
10 Figure 6. This will measure the precision of the generated quasi-static and high-rate experimental  
11 results. The verification process employs the force-displacement results of an ENF experiment. In  
12 a standard fashion, the force is obtained from the testing machine readings while the displacement  
13 is measured *via* DIC – these will be used as the benchmark. If the force-displacement readings  
14 generated with the new method match these benchmarks, the newly developed measurement tech-  
15 nique is assumed verified and therefore valid for the measurement of both quasi-static and dynamic  
16 loading regimes.

17 However, these standard equations – which were developed for quasi-static loading conditions  
18 based on the simple beam theory (SBT) – need also to be proven in a high-rate loading regime.  
19 This is accomplished by focusing on the deflection of an adherent arm and by the determination  
20 of characteristic times. The compliance of one adherent arm of a WDCB experiment is calculated  
21 both for the quasi-static and the dynamic loading case – see Figure 7. When a match between both  
22 loading regimes is achieved, one can assume that the equations derived from QS equilibrium are  
23 valid for high-rate analysis.

24 For the experiments one needs to calculate the characteristic times of the structures explained  
25 in detail by Delvare *et al.* [52]. These characteristics times can be defined as: (i) reference time,  
26  $T_R$ , (ii) characteristic time,  $T_T$  and (iii) support reaction time,  $T_C$ .  $T_R$  is the effective duration of  
27 the test and corresponds to the elapsed time when the incident wave reaches the specimen and the  
28 fracture of the specimen.  $T_T$  represents the first response of the beam – which is defined by the



1 duration of a round trip of the elastic wave,  $c$ , across the width of the specimen  $h$ , following

$$T_T = \frac{2h + t_a}{c} \quad (20)$$

2 where  $t_a$  is the thickness of the adhesive. Finally,  $T_C$  is related to the duration of the wave  
3 travelling from the impact location to the end of the specimen and back – this is described following

$$T_C = \frac{L}{c} . \quad (21)$$

4 where  $L$  is the characteristic length of the specimen.

5 With a rough estimation of the characteristic times, it is possible to identify whether the exper-  
6 iments are in equilibrium. If it can be assumed that the specimens are in a dynamic equilibrium,  
7 the standard equations in Section 2 and summarised in Table 2 are applicable. This would mean  
8 that the supports are aware of each other’s existence and that the force of the impactor (loading  
9 pin) is twice the force of the supports.

10 ENF experiments performed under QS conditions are analysed using the standard and the new  
11 measuring technique. Figure 7(a) compares the force-displacement results recorded directly from  
12 the testing apparatus against the force-displacement extracted using DIC exclusively. Both force-  
13 displacement curves are in excellent agreement and shows the ability of the new method to capture  
14 the failure point with precision. This verifies the new method for high-rate experiments – if one  
15 assumes that the elastic deformation of the adherents is rate independent. This is supported by  
16 Figure 7(b), which shows that the adherents’ compliance of a WDCB specimen is rate independent:  
17 the deflection of one beam in QS (black lines) and HR (blue lines) are obtained and compared with  
18 each other. No major deviation is observed. Additionally, the characteristic times reveal that the  
19 reference time ( $T_R = 500 \mu\text{s}$ ) is large enough when compared to  $T_T$  and  $T_C$  ( $1.46 \mu\text{s}$  and  $23 \mu\text{s}$   
20 respectively). Therefore, one may consider that the HR experiments exhibit a dynamic equilibrium,  
21 thus allowing the use of the standard equations for calculating the necessary fracture parameters.

#### 22 4.2. Experimental results: WDCB, ENF, and SLB

23 The results for the three investigated deformation modes experimented under QS and HR are  
24 summarised in Figure 8. The quasi-static force results for the WDCB experiments have a mean  
25 fracture force of  $F = 983 \text{ N}$  with a standard deviation of  $s = 6.8 \%$ . On the other hand, the QS

1 ENF experiments result in a mean fracture force of  $F = 4018$  N with a standard deviation of  $s =$   
2 6.6 %. For the same loading regime, the SLB experiments show a mean fracture force of  $F = 2071$   
3 with  $s = 8.2$  %. As expected the mixed-mode experimental results represented by SLB specimens  
4 are larger than the mode I values (represented by WDCB specimens) but smaller than the mode  
5 II results (represented by the ENF specimens).

6 Accordingly, HR results of the WDCB experiments show a mean fracture force of  $F = 540$  N  
7 with  $s = 16.8$  %, while the ENF experiments result in a mean fracture force of  $F = 2927.5$  N with  
8  $s = 13.4$  %. Also, the HR SLB experiment values of  $F = 1486$  N and  $s = 7.9$  % are larger than  
9 the HR WDCB ones but smaller than the HR ENF values. The standard deviation up to  $s = 16$   
10 % can be explained with the composition of the adhesive interface. Voids and imperfections within  
11 the adhesive interface are believed to cause scatter in mechanical performance. A negative rate-  
12 dependency of the force-displacement curves follow previous observations: the dissipated energy of  
13 the adhesive tends to decrease with an increase of deformation rate.

#### 14 *4.3. Rate-dependent fracture energy*

15 This subsection quantifies the fracture energy,  $J$ , as a function of the different fracture modes  
16 and loading rates.

17 Employing Eqs.13, 14, 15, and 16, the fracture energy for each deformation mode and loading  
18 regime is calculated and presented in Figure 9. HR fracture energies for each different deformation  
19 mode are lower than the obtained values in the QS regime. The relevant values of fracture energy  
20 and standard deviations are summarised in Table 3. It is shown that the QS measured fracture  
21 energies are within the trend of the results investigated by Alvarez [51] using similar methods.  
22 One should note that the results from [51] were obtained using different adhesive thicknesses and  
23 specimen geometries than the current study. Nevertheless, there is a close agreement between them.  
24 Moreover, Figure 10 also compares the measured values of this study against those measured by the  
25 authors using butt joint, single lap joint and scarf joint experiments [15]. The difference between  
26 these characterisation experiments and the fracture mechanics experiments are rationalised in a  
27 later section.

28 Finally, a rate dependent failure envelope using the measured fracture energies is generated  
29 and presented in Figure 11. Based on the Benzeggagh-Kenan (BK) and power law criterion, the  
30 relationship between the modes of failure can be obtained for both QS and HR regimes. This

Table 3: Mean value and standard deviation of the fracture energy, J (N/mm), for QS and HR regimes, and the three different fracture modes.

Rate	WDCB	ENF	SLB
QS	$3.68 \pm 0.53$	$8.40 \pm 1.20$	$3.83 \pm 0.40$
HR	$1.43 \pm 0.25$	$4.50 \pm 0.36$	$1.50 \pm 0.26$

1 failure envelope enables design engineers to interpolate the measured fracture behaviour in the  
 2 most appropriate loading conditions.

#### 3 *4.4. Fractography analysis: on the nature of failure*

4 In order to assure that the measured fracture energies belong to the adhesive interface, it was  
 5 necessary to study in detail the fracture surface of the tested specimens. Thus, the fractured sur-  
 6 faces of representative specimens were investigated with a 3D optical microscope (Alicona). The  
 7 profilometer allows one to reconstruct three-dimensionally and with great precision the fracture  
 8 surface of the samples. Figure 12 shows optical micrographs for each deformation mode and load-  
 9 ing rate. Moreover, the profile height of each surface was measured in order to determine whether  
 10 cohesive failure within the adhesive interface or adhesion failure at the interface between adherent  
 11 and adhesive occurred. The profile lines presented in Figure 12 show average heights of approxi-  
 12 mately 0.15 to 0.20 mm. Given that the adhesive measures approximately 0.25 mm in thickness,  
 13 it is reasonable to believe that cohesive failure is dominant. The optical micrographs also reveal  
 14 the presence of adhesive at both sides of the specimen. Moreover, optical analysis also reveals the  
 15 existence of voids and carrier fibres. These have been considered previously [15] as important fea-  
 16 tures that contribute to the failure behaviour of the adhesive interface. Finally, the higher fracture  
 17 energy observed in ENF specimens is believed due to multiple micro-crack creation ahead the crack  
 18 tip, subsequent coalescence, and increase in friction of the surfaces resulting in additional energy  
 19 absorption.

## 20 **5. Numerical method**

21 One of the objectives of the present work is to employ fracture mechanics experiments to validate  
 22 a cohesive zone model (CZM) – which was calibrated using butt joint, single lap joint and scarf  
 23 joint experiments [15] (also named characterisation experiments from here onwards). Models of

1 this kind are often used in finite element analysis to simulate and predict the behaviour of complex  
 2 adhesively bonded structures. Figure 13 demonstrates the process which has been followed to prove  
 3 the models ability to predict failure. This section also details the setup of the finite element models  
 4 developed for the WDCB, ENF, and SLB experiments (also named fracture mechanics experiments  
 5 from here onwards). The behaviour of the adhesive employed has been previously measured and  
 6 modelled in the form of a CZM in previous work from the authors. The CZM is summarised next.

### 7 5.1. Material model

8 The CZM developed allows the modelling of a rate, thickness, and deformation mode dependent  
 9 traction separation law (TSL) for adhesive interfaces following a trapezoidal shape. Figure 13 shows  
 10 the used nomenclature for representing the model. The plateau area represents plastic deformation  
 11 caused by crack initiation, crack nucleation and crack coalescences. The whole area under the TSL  
 12 curve is presented by the dissipated energy. The model characteristic rate-dependent parameters  
 13 are explained next.

14 The rate dependent peak stress for the mode I and mode II contributions are implemented  
 15 following a logarithmic function expressed as

$$T_N(\dot{\epsilon}_N, f_v) = \left[ T_{\text{refN}} + T_{0N} \cdot \ln \left( \frac{\dot{\epsilon}_N}{\dot{\epsilon}_{\text{ref}}} \right) \right] \cdot (1 - f_v) \quad (22)$$

16 and

$$T_S(\dot{\epsilon}_S, f_v) = \left[ T_{\text{refS}} + T_{0S} \cdot \ln \left( \frac{\dot{\epsilon}_S}{\dot{\epsilon}_{\text{ref}}} \right) \right] \cdot (1 - f_v) \quad (23)$$

17 where,  $T_{\text{refN}}$ ,  $T_{\text{refS}}$  and  $T_{0N}$ ,  $T_{0S}$  are the reference values of peak stress and the strain rate  
 18 sensitivity parameters respectively. The parameter  $\dot{\epsilon}_{\text{ref}}$  is the reference strain rate, and  $\dot{\epsilon}_i$  is the  
 19 updated strain rate for  $i = N, S$  which represent mode I and mode II respectively. The parameter  $f_v$   
 20 represents the void volume fraction which has been defined in previous studies [15] to be dependent  
 21 on the adhesive interface thickness. It is expressed with

$$f_v(t_a) = f_{vref} \cdot t_a^{-f_{v0}} \quad (24)$$

22 where  $f_{vref}$  is the reference value and  $f_{v0}$  is the thickness sensitivity parameter.

1 Similarly, the dissipated energy (fracture energy) also follows a logarithmic function which can  
 2 be written for mode I as

$$G_{cN}(\dot{\epsilon}_N, f_v) = \left[ G_{\text{refN}} - G_{0N} \cdot \ln \left( \frac{\dot{\epsilon}_N}{\dot{\epsilon}_{\text{ref}}} \right) \right] \cdot (1 - f_v) \cdot \left( 1 - \frac{t_0}{t_a} \right) \quad (25)$$

3 while the mode II dissipated energy  $G_{cS}$  is described as:

$$G_{cS}(\dot{\epsilon}_S, f_v) = \left[ G_{\text{refS}} - G_{0S} \cdot \ln \left( \frac{\dot{\epsilon}_S}{\dot{\epsilon}_{\text{ref}}} \right) \right] \cdot (1 - f_v) \cdot \left( 1 - \frac{t_0}{t_a} \right) \quad (26)$$

4 where  $G_{\text{refN}}$  and  $G_{\text{refS}}$  are the reference values of the dissipated energy in mode I and mode II  
 5 respectively, and  $G_{0N}$  and  $G_{0S}$  represent the strain rate sensitivity parameters for each mode. The  
 6 parameter  $t_0$  describes the thickness reference value.

7 Since previous experimental observations suggest a rate dependent behaviour of the plateau area  
 8 it is considered in the model. This was done by introducing a plateau ratio which represents the  
 9 relationship between the plateau area and the dissipated energy. According to

$$P_N(\dot{\epsilon}_N) = P_{\text{refN}} \cdot \left( \frac{\dot{\epsilon}_N}{\dot{\epsilon}_{\text{ref}}} \right)^{p_N} \quad (27)$$

10 and

$$P_S(\dot{\epsilon}_S) = P_{\text{refS}} \cdot \left( \frac{\dot{\epsilon}_S}{\dot{\epsilon}_{\text{ref}}} \right)^{p_S} \quad (28)$$

11 the plateau ratios for mode I and II are described, respectively. The parameters  $P_{\text{refN}}$  and  $P_{\text{refS}}$   
 12 are the reference values for mode I and mode II respectively, and  $p_N$  and  $p_S$  are the strain rate  
 13 sensitivity parameters of the plateau ratio.

14 In the following the shape given parameters for the CZM are explained: The mixed-mode  
 15 behaviour of the TSL is defined by a quadratic criterion for the yielding initiation expressed as

$$\left( \frac{\delta_{m1,I}}{\delta_{n1}} \right)^2 + \left( \frac{\delta_{m1,II}}{\delta_{s1}} \right)^2 = 1, \quad (29)$$

16 while a linear criterion describes the damage initiation and final failure using the expression

$$\left( \frac{\delta_{mi,I}}{\delta_{ni}} \right) + \left( \frac{\delta_{mi,II}}{\delta_{si}} \right) = 1 \quad i = 2, f \quad (30)$$

1 The yield initiation  $\delta_{m1}$  can be calculated using the expression

$$\delta_{m1} = \delta_{n1} \delta_{s1} \sqrt{\frac{1 + \beta^2}{\delta_{s1}^2 + (\delta_{n1} \beta)^2}} \quad (31)$$

2 considering an equivalent mixed-mode displacement

$$\delta_{m1} = \sqrt{\delta_{m1,I}^2 + \delta_{m1,II}^2} \quad (32)$$

3 and a mixed-mode ratio with

$$\beta = \frac{\delta_{m1,II}}{\delta_{m1,I}} . \quad (33)$$

4 The yield initiation displacement is then fully described with the relevant displacements for each  
5 mode separately. This is described following

$$\delta_{n1} = \frac{T_N}{K_n} \quad \text{and} \quad \delta_{s1} = \frac{T_S}{K_s} \quad (34)$$

6 where the indices  $n$  and  $s$  represent mode I and mode II respectively. The stiffness for each  
7 mode is calculated with

$$K_n = \frac{E}{t_{el}} \quad \text{and} \quad K_s = \frac{G}{t_{el}} \quad (35)$$

8 where  $E$  is the Young's modulus (2000 MPa) of the adhesive,  $G$  the shear modulus of the  
9 adhesive (220 MPa), and  $t_{el}$  the element thickness.

10 The damage initiation  $\delta_{m2}$  and the final failure displacement  $\delta_{mf}$  are described in a similar way  
11 using

$$\delta_{mi} = \delta_{ni} \delta_{si} \frac{\sqrt{1 + \beta^2}}{(\beta \delta_{ni} + \delta_{si})} \quad i = 2, f . \quad (36)$$

12 The relevant mode I and II dependent components for the damage initiation are described by

$$\delta_{n2} = \delta_{n1} + \frac{2 \cdot G_{cN} \cdot P_N}{T_N \cdot (1 + \gamma_N)} \quad \text{and} \quad \delta_{s2} = \delta_{s1} + \frac{2 \cdot G_{cS} \cdot P_N}{T_S \cdot (1 + \gamma_S)} . \quad (37)$$

1 while the mode I and II components for the final failure displacement are expressed as

$$\delta_{nf} = \delta_{n1} + \delta_{n2} + \frac{2 \cdot G_{cN}}{T_N \cdot \gamma_N} - \frac{\delta_{n2} + \gamma_N \cdot (\delta_{n2} - \delta_{n1})}{\gamma_N} \quad (38)$$

2 and

$$\delta_{sf} = \delta_{s1} + \delta_{s2} + \frac{2 \cdot G_{cS}}{T_S \cdot \gamma_S} - \frac{\delta_{s2} + \gamma_S \cdot (\delta_{s2} - \delta_{s1})}{\gamma_S} \quad (39)$$

3 where the parameters  $\gamma_N$  and  $\gamma_S$  enable the representation of a softening plateau area. These  
4 parameters represent a fraction of the maximum traction described by

$$t = (1 - d)K\delta . \quad (40)$$

5 Then, the damage  $d$  can be fully defined as

$$d = \begin{cases} 0 & , \delta \leq \delta_{m1} \\ 1 - \frac{\delta_{m1}}{\delta_m} \cdot \left[ 1 + \frac{(\gamma_m - 1)(\delta_m - \delta_{m1})}{(\delta_{m2} - \delta_{m1})} \right] & , \delta_{m1} < \delta \leq \delta_{m2} \\ 1 - \left[ \frac{\gamma_m \cdot \delta_{m1}}{\delta_m} \cdot \frac{(\delta_{mf} - \delta_m)}{(\delta_{mf} - \delta_{m2})} \right] \cdot \left[ 2 \cdot \left( \frac{\delta - \delta_{m2}}{\delta_{mf} - \delta_{m2}} \right)^3 - 3 \cdot \left( \frac{\delta - \delta_{m2}}{\delta_{mf} - \delta_{m2}} \right)^2 + 1 \right] & , \delta_{m2} < \delta \leq \delta_{mf} \\ 1 & , \delta > \delta_f \end{cases} \quad (41)$$

6 where  $\gamma_m$  represents the percentage of plateau decrease for the mixed mode case and that follows

$$\gamma_m = \sqrt{\frac{\gamma_N^2 + (\beta \cdot \gamma_S)^2}{(1 + \beta^2)}} . \quad (42)$$

7 Consequently, the traction-separation relationship following Eq.40 is fully described by con-  
8 sidering that the stiffness  $K$  of the structure also includes the influence of mode I and mode II  
9 employing

$$K = \sqrt{\frac{K_n^2 + (\beta \cdot K_s)^2}{(1 + \beta^2)}} \quad (43)$$

10 The material parameters of the AF 163-2OST adhesive are summarised in Table 4

Table 4: Material model properties for the AF 163-2OST adhesive.

$E(\text{MPa})$	$G(\text{MPa})$	$T_{refN}(\text{MPa})$	$T_{0N}$	$G_{refN}(\text{N/mm})$	$G_{0N}$	$P_{refN}$
2000	220	38.00	1.90	5.6	0.23	0.65
$p_N$	$\gamma_N$	$T_{refS}(\text{MPa})$	$T_{0S}$	$G_{refS}(\text{N/mm})$	$G_{0S}$	$P_{refS}$
-0.01	1.00	36.00	1.80	13.65	0.25	0.80
$p_S$	$\gamma_S$	$f_{vref}$	$f_{v0}$	$t_0$		
-0.03	0.85	0.54	0.02	0.038		

## 5.2. Numerical setup

Simulations of the investigated deformation modes were performed to validate the CZM developed previously by the authors [15] and summarised above. In order to validate the CZM by comparing to the experiments, the same boundary and loading conditions must be applied. The simulations were carried out in 3D using the finite element solver Abaqus/Standard. C3D8 elements were used to discretise the adherents. The adhesive interface was modelled using 3D cohesive elements with 4 integration points by modelling the adhesive thickness geometrically. Each specimen configuration modelled follows the dimensions used in the experiments. The size of the elements for adherents and adhesive parts were 0.5 x 0.5 x 0.5 and 0.3 x 0.5 x 0.5 mm in thickness, width and length respectively. For the boundary conditions, the end of the WDCB specimen has been restricted in all the degrees of freedom (DOF). A friction coefficient of 0.1 was chosen between the wedge and the specimen arms. This was verified by comparing the experimental and numerically obtained wedge-force. Additionally, the ENF and SLB experiments were modelled with a friction coefficient of 0.1 between the specimen and the supports. The movement of the lower supports were restricted in all DOF while the loading pin was restricted in all DOF apart from the loading direction. The velocity was applied at the corresponding loading pin for the WDCB, ENF and SLB experimental setups. The simulation setups are summarised in Figure 14.

## 6. Numerical results

The traction-separation behaviour of the model is illustrated in Figure 15 for different rates and loading modes. Both experimental results from previous characterisation experimentation [15] and CZM are shown. Our goal is to use the fracture mechanic results to validate the model. This validation process is critical, particularly when one intends to use their interpolation capacity.



1 Here, we use the newly developed measuring technique to validate the adhesive CZM both under  
2 quasi-static and dynamic loading regimes.

3 Figures 16, 17 and 18 compare the experimental and simulated behaviour of the WDCB, ENF,  
4 and SLB tests respectively. Simulations show good agreement to the experimental results – these  
5 are able to capture both the rate and the deformation mode dependence of the fracture process.  
6 **No significant mesh size dependency on the numerical results was observed.** Figures 16, 17 and 18  
7 show the results for each fracture mode in 3D. Additionally, the graphs show the displacement field  
8 of experiments and models at different points during the fracture process – these are highlighted  
9 accordingly in the force-displacement curves. It is observed that the simulations slightly over-predict  
10 the experimental results. Nevertheless, it is reasonable to believe that both are in reasonable good  
11 agreement. The deviation between the simulation and the average experimental results in QS is  
12 12.9 %, 13.0 % and 18.0 % while in HR it is 20.0 %, 18.0 % and 16.0 % for WDCB, ENF and SLB  
13 respectively. This over prediction can be explained when comparing the fracture energy values for  
14 the characterisation and fracture mechanics experiments in mode I and mode II loading. Figure 19  
15 shows that the model is overpredicting when comparing with the values of the fracture mechanics  
16 experiments.

17 In order to quantify this difference, some simple inverse modelling is carried out. It was found  
18 that lowering the reference values of the model dissipated energy greatly improves the agreement  
19 between models and fracture mechanics experiments. The value  $G_{refN}$  (N/mm) was reduced from  
20 4.3 to 3 N/mm and the value for  $G_{refS}$  (S/mm) from 10.5 to 9 N/mm. Results are presented and  
21 compared in Figure 19. Simulations with reduced reference energies result in an improved prediction  
22 of the experimentally obtained force-displacement curves for the WDCB, ENF and SLB experiments  
23 – these are shown in Figure 20. These results prove that the characterisation experiments are able to  
24 accurately capture the peak traction of the adhesive. In terms of energy measurements, a difference  
25 between characterisation and fracture mechanics experiments between 10 and 20 % is observed –  
26 depending on the loading mode.

27 This over-prediction of the energy by the characterisation experiments might be due to several  
28 reasons: (i) boundary edge effects exist in the characterisation experiments but not in the fracture  
29 mechanics experiments (due to the miniaturised nature of the characterisation experiments), (ii)  
30 small experimental measurement deviation in either of the experimental approaches, (iii) differences  
31 in thickness, (iv) differences in the surface specimen preparation, (v) different amounts of porosity,

1 (vi) additional failure mechanisms such as fibre debonding or fibre pull-out which are not accounted  
2 for in the model or (vii) a combination of all of the above. Nevertheless, the discrepancies are small.  
3 Our results are useful in validating and improving the proposed cohesive zone model. The modelling  
4 work also helps in assessing and reinforcing the new measurement technique for dynamic fracture  
5 mechanics experiments. The technique outlined here provides a valid and comparatively simple  
6 approach to analyse high-rate deformation of adhesively bonded structures.

## 7 **7. Conclusions**

8 This work investigates the rate-dependence of fracture mechanics experiments in the form of the  
9 WDCB, ENF and SLB experiments by proposing a new measuring technique valid for both quasi-  
10 static and dynamic experimentation. These experiments impose mode I, mode II and mixed-mode  
11 I/II loading on the joint respectively. Experimental results are then used to validate a CZM of the  
12 adhesive interface. The following conclusions can be drawn from this work:

- 13 1. A novel measurement technique that can be used in dynamic environments is developed. This  
14 relies entirely upon DIC, thus circumventing any dynamic effect during experimentation. This  
15 method is successfully verified in the quasi-static and high-rate loading regimes by comparing  
16 directly to standard measuring techniques in QS and by comparing the compliance between  
17 QS and HR measurements.
- 18 2. This method is then used to measure the rate- and fracture-mode dependent mechanical  
19 properties of a structural adhesive interface under QS and HR regimes. Analysis reveals the  
20 maximum force and dissipated energy of the adhesive structures.
- 21 3. The experimental results for the three different modes of fracture mechanics experiments  
22 revealed a negative rate-dependent behaviour for the force-displacement curves – the fracture  
23 energy exhibited a decrease with increasing loading rate.
- 24 4. Fractography analysis showed that the adhesive fracture is predominantly cohesive in nature.  
25 This gave further validity to the fracture energy results – it is reasonable that these belong  
26 to the adhesive interface itself and not the interface between the metal and the adhesive.
- 27 5. Numerical modelling of the experiments is used to validate a CZM of the adhesive. This  
28 was previously characterised with smaller scale specimens. The simulated results were able  
29 to predict the experiments accurately. The combination of small scale experiments and large

30 scale fracture mechanics experiments provide a flexible and powerful framework for the study  
1 of adhesives loaded both quasi-statically and dynamically.

## 2 **Acknowledgements**

3 The authors of this paper are grateful to Jeffrey Fullerton and Stuart Carter, Impact Engineering  
4 Laboratory, University of Oxford, for their assistance in the manufacturing of the specimens. The  
1 authors acknowledge the funding from Rolls-Royce plc which enabled this investigation.

2 **References**

3 **References**

- 4 [1] M. D. Banea, L. F. Da Silva, Adhesively bonded joints in composite materials: An overview,  
5 Proceedings of the Institution of Mechanical Engineers, Part L: Journal of Materials: De-  
6 sign and Applications 223 (1) (2009) 1–18. arXiv:arXiv:1011.1669v3, doi:10.1243/  
7 14644207JMDA219.
- 8 [2] J. J. M. Machado, E. A. S. Marques, L. F. M. da Silva, Adhesives and adhesive joints under  
9 impact loadings: An overview, The Journal of Adhesion 94 (6) (2018) 421–452. doi:10.1080/  
10 00218464.2017.1282349.  
11 URL <https://doi.org/10.1080/00218464.2017.1282349>
- 12 [3] T. Yokoyama, H. Shimizu, Evaluation of Impact Shear Strength of Adhesive Joints with the  
13 Split Hopkinson Bar, JSME International Journal 41 (4) (1998) 503–509.
- 14 [4] M. May, O. Hesebeck, S. Marzi, W. Böhme, J. Lienhard, S. Kilchert, M. Brede, S. Hiermaier,  
15 Rate dependent behavior of crash-optimized adhesives – Experimental characterization, model  
16 development, and simulation, Engineering Fracture Mechanics 133 (2015) 112–137. doi:10.  
17 1016/j.engfracmech.2014.11.006.  
18 URL <http://linkinghub.elsevier.com/retrieve/pii/S0013794414003804>
- 19 [5] T. Yokoyama, K. Nakai, Determination of the impact tensile strength of structural adhesive  
20 butt joints with a modified split Hopkinson pressure bar, International Journal of Adhesion  
21 and Adhesives 56 (2015) 13–23. doi:10.1016/j.ijadhadh.2014.07.011.  
22 URL <http://dx.doi.org/10.1016/j.ijadhadh.2014.07.011>
- 23 [6] T. Yokoyama, Experimental determination of impact tensile properties of adhesive butt joints  
24 with the split Hopkinson bar, The Journal of Strain Analysis for Engineering Design 38 (3)  
25 (2003) 233–245. doi:10.1243/030932403765310563.  
26 URL [http://journals.pepublishing.com/openurl.asp?genre=article&id=doi:  
27 10.1243/030932403765310563](http://journals.pepublishing.com/openurl.asp?genre=article&id=doi:10.1243/030932403765310563)
- 28 [7] S. L. Raykhere, P. Kumar, R. Singh, V. Parameswaran, Dynamic shear strength of adhesive  
1 joints made of metallic and composite adherents, Materials & Design 31 (4) (2010) 2102–2109.

- 2       doi:10.1016/j.matdes.2009.10.043.  
3       URL <http://linkinghub.elsevier.com/retrieve/pii/S0261306909005974>
- 4   [8] M. Y. Tsai, J. Morton, An investigation into the stresses in double-lap adhesive joints with  
5       laminated composite adherends, *International Journal of Solids and Structures* 47 (24) (2010)  
6       3317–3325. doi:10.1016/j.ijsolstr.2010.08.011.  
7       URL <http://dx.doi.org/10.1016/j.ijsolstr.2010.08.011>
- 8   [9] M. Lißner, E. Alabort, H. Cui, A. Pellegrino, N. Petrinic, On the rate dependent behaviour of  
9       epoxy adhesive joints: Experimental characterisation and modelling of mode I failure, *Com-  
10       posite Structures* 189 (2018) 286–303. doi:10.1016/j.compstruct.2018.01.019.  
11       URL <https://doi.org/10.1016/j.compstruct.2018.01.019>
- 12 [10] A. M. Pinto, A. G. Magalhães, R. D. Campilho, M. F. de Moura, A. P. Baptista, Single-lap  
13       joints of similar and dissimilar adherends bonded with an acrylic adhesive, *Journal of Adhesion*  
14       85 (6) (2009) 351–376. doi:10.1080/00218460902880313.
- 15 [11] S. Sassi, M. Tarfaoui, H. B. Yahia, Thermomechanical behavior of adhesively bonded joints  
16       under out-of-plane dynamic compression loading at high strain rate, *Journal of Composite*  
17       *Materials* 52 (30) (2018) 4171–4184. doi:10.1177/0021998318777048.
- 18 [12] S. Sassi, M. Tarfaoui, H. Benyahia, Experimental study of the out-of-plane dynamic behaviour  
19       of adhesively bonded composite joints using split Hopkinson pressure bars, *Journal of Com-  
20       posite Materials* 52 (21) (2018) 2875–2885. doi:10.1177/0021998318758368.
- 21 [13] S. Sassi, M. Tarfaoui, H. Ben Yahia, An investigation of in-plane dynamic behavior of  
22       adhesively-bonded composite joints under dynamic compression at high strain rate, *Composite*  
23       *Structures* 191 (2018) 168–179. doi:10.1016/j.compstruct.2018.02.057.
- 24 [14] S. Sassi, M. Tarfaoui, H. Ben Yahia, In-situ heat dissipation monitoring in adhesively bonded  
25       composite joints under dynamic compression loading using SHPB, *Composites Part B: Engi-  
26       neering* 154 (July) (2018) 64–76. doi:10.1016/j.compositesb.2018.07.039.  
27       URL <https://doi.org/10.1016/j.compositesb.2018.07.039>
- 28 [15] M. Lißner, E. Alabort, H. Cui, R. Rito, B. Blackman, N. Petrinic, Experimental charac-  
1       terisation and numerical modelling of the influence of bondline thickness, loading rate, and

- 2 deformation mode on the response of ductile adhesive interfaces, *Journal of the Mechanics and*  
3 *Physics of Solids* 130 (2019) 349–369. doi:10.1016/j.jmps.2019.06.011.
- 4 [16] B. R. K. Blackman, A. J. Kinloch, F. S. Rodriguez Sanchez, W. S. Teo, J. G. Williams, The  
5 fracture behaviour of structural adhesives under high rates of testing, *Engineering Fracture*  
6 *Mechanics* 76 (18) (2009) 2868–2889. doi:10.1016/j.engfracmech.2009.07.013.  
7 URL <http://linkinghub.elsevier.com/retrieve/pii/S0013794409002380>
- 8 [17] J. Neumayer, P. Kuhn, H. Koerber, R. Hinterhölzl, Experimental Determination of the Tensile  
9 and Shear Behaviour of Adhesives under Impact Loading, *The Journal of Adhesion* 92 (7-9)  
10 (2015) 503–516. doi:10.1080/00218464.2015.1092387.  
11 URL [http://www.scopus.com/inward/record.url?eid=2-s2.](http://www.scopus.com/inward/record.url?eid=2-s2.0-84962339117&partnerID=tZ0tx3y1)  
12 [0-84962339117&partnerID=tZ0tx3y1](http://www.scopus.com/inward/record.url?eid=2-s2.0-84962339117&partnerID=tZ0tx3y1)
- 13 [18] J. Wiegand, A. Hornig, R. Gerlach, C. Neale, N. Petrinic, W. Hufenbach, An experimental  
14 method for dynamic delamination analysis of composite materials by impact bending, *Mechan-*  
15 *ics of Advanced Materials and Structures* 22 (5) (2015) 413–421. doi:10.1080/15376494.  
16 2012.736066.
- 17 [19] M. Yasaee, G. Mohamed, A. Pellegrino, N. Petrinic, S. R. Hallett, Strain rate dependence of  
18 mode II delamination resistance in through thickness reinforced laminated composites, *Inter-*  
19 *national Journal of Impact Engineering* 107 (May) (2017) 1–11. doi:10.1016/j.ijimpeng.  
20 2017.05.003.
- 21 [20] M. Isakov, M. May, P. Hahn, H. Paul, M. Nishi, Fracture toughness measurement without  
22 force data – Application to high rate DCB on CFRP, *Composites Part A: Applied Science and*  
23 *Manufacturing* 119 (January) (2019) 176–187. doi:10.1016/j.compositesa.2019.01.030.  
24 URL <https://doi.org/10.1016/j.compositesa.2019.01.030>
- 25 [21] S. A. Ponnusami, M. V. Pathan, H. Cui, B. Erice, N. Petrinic, A Wedge-DCB Test Methodology  
26 to Characterise High Rate Mode-I Interlaminar Fracture Properties of Fibre Composites, *EPJ*  
27 *Web of Conferences* 183 (January) (2018). doi:10.1051/epjconf/201818302052.
- 28 [22] B. R. K. Blackman, A. J. Kinloch, M. Paraschi, W. S. Teo, Measuring the mode I adhesive  
1 fracture energy, GIC, of structural adhesive joints: The results of an international round-

- 2 robin, *International Journal of Adhesion and Adhesives* 23 (4) (2003) 293–305. doi:10.1016/  
3 S0143-7496(03)00047-2.
- 4 [23] D. Álvarez, B. R. K. Blackman, F. J. Guild, A. J. Kinloch, Mode I fracture in adhesively-bonded  
5 joints: A mesh-size independent modelling approach using cohesive elements, *Engineering*  
6 *Fracture Mechanics* 115 (2014) 73–95. doi:10.1016/j.engfracmech.2013.10.005.
- 7 [24] M. F. De Moura, N. Dourado, J. J. Morais, F. A. Pereira, Numerical analysis of the ENF  
8 and ELS tests applied to mode II fracture characterization of cortical bone tissue, *Fatigue*  
9 *and Fracture of Engineering Materials and Structures* 34 (3) (2011) 149–158. doi:10.1111/  
10 j.1460-2695.2010.01502.x.
- 11 [25] J. M. Oliveira, M. F. De Moura, J. J. Morais, Application of the end loaded split and single-  
12 leg bending tests to the mixed-mode fracture characterization of wood, *Holzforschung* 63 (5)  
13 (2009) 597–602. doi:10.1515/HF.2009.088.
- 14 [26] L. F. M. da Silva, V. H. C. Esteves, F. J. P. Chaves, Fracture toughness of a structural adhesive  
15 under mixed mode loadings, *Materialwissenschaft und Werkstofftechnik* 42 (5) (2011) 460–470.  
16 doi:10.1002/mawe.201100808.
- 17 [27] Y. Yamagata, X. Lu, Y. Sekiguchi, C. Sato, Experimental investigation of mode I fracture  
18 energy of adhesively bonded joints under impact loading conditions, *Applied Adhesion Science*  
19 5 (7) (2017) 1–10. doi:10.1186/s40563-017-0087-7.
- 20 [28] D. A. Dillard, D. J. Pohlit, G. C. Jacob, J. M. Starbuck, R. K. Kapania, On the use of a  
21 driven wedge test to acquire dynamic fracture energies of bonded beam specimens, *Journal of*  
22 *Adhesion* 87 (4) (2011) 395–423. doi:10.1080/00218464.2011.562125.
- 23 [29] N. Aurore, J. Julien, Double cantilever beam tests on a viscoelastic adhesive: effects of the  
24 loading rate, *Procedia Structural Integrity* 2 (2016) 269–276. doi:10.1016/j.prostr.2016.  
25 06.035.  
26 URL <http://dx.doi.org/10.1016/j.prostr.2016.06.035>
- 27 [30] T. Andersson, U. Stigh, The stress-elongation relation for an adhesive layer loaded in peel using  
28 equilibrium of energetic forces, *International Journal of Solids and Structures* 41 (2) (2004)  
1 413–434. doi:10.1016/j.ijsolstr.2003.09.039.

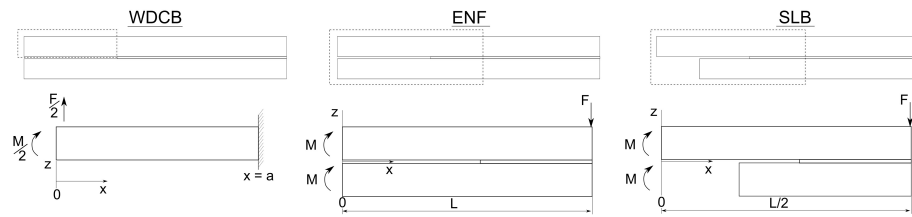
- 2 [31] B. R. Blackman, A. J. Kinloch, M. Paraschi, The determination of the mode II adhesive fracture  
3 resistance, GIIC, of structural adhesive joints: An effective crack length approach, *Engineering*  
4 *Fracture Mechanics* 72 (6 SPEC. ISS.) (2005) 877–897. doi:10.1016/j.engfracmech.2004.  
5 08.007.
- 6 [32] M. F. De Moura, Numerical simulation of the ENF test for the mode-II fracture characterization  
7 of bonded joints, *Journal of Adhesion Science and Technology* 20 (1) (2006) 37–52. doi:  
8 10.1163/156856106775212422.
- 9 [33] M. F. de Moura, M. A. Silva, A. B. de Morais, J. J. Morais, Equivalent crack based mode  
10 II fracture characterization of wood, *Engineering Fracture Mechanics* 73 (8) (2006) 978–993.  
11 doi:10.1016/j.engfracmech.2006.01.004.
- 12 [34] M. Alfano, R. E. Link, G. H. Paulino, L. Pagnotta, F. Furgiuele, M. R. Mitchell, Analysis  
13 of Fracture in Aluminum Joints Bonded with a Bi-Component Epoxy Adhesive, *Journal of*  
14 *Testing and Evaluation* 39 (2) (2010) 102753. doi:10.1520/jte102753.
- 15 [35] C. Sarrado, A. Turon, J. Costa, J. Renart, On the validity of linear elastic fracture mechanics  
16 methods to measure the fracture toughness of adhesive joints, *International Journal of Solids*  
17 *and Structures* 81 (2015) 110–116. doi:10.1016/j.ijsolstr.2015.11.016.
- 18 [36] Y. Sekiguchi, M. Katano, C. Sato, Experimental study of the Mode I adhesive fracture energy  
19 in DCB specimens bonded with a polyurethane adhesive, *Journal of Adhesion* 93 (3) (2017)  
20 235–255. doi:10.1080/00218464.2015.1070101.  
21 URL <http://dx.doi.org/10.1080/00218464.2015.1070101>  
22 <https://doi.org/10.1080/00218464.2015.1070101>
- 23 [37] J. Xavier, J. Morais, N. Dourado, M. F. De Moura, Measurement of mode I and mode II fracture  
24 properties of wood-bonded joints, *Journal of Adhesion Science and Technology* 25 (20) (2012)  
25 2881–2895. doi:10.1163/016942411X576563.
- 26 [38] L. F. Da Silva, F. A. De Magalhães, F. J. Chaves, M. F. De Moura, Mode II fracture toughness  
27 of a brittle and a ductile adhesive as a function of the adhesive thickness, *Journal of Adhesion*  
1 86 (9) (2010) 889–903. doi:10.1080/00218464.2010.506155.



- 2 [39] M. F. S. F. de Moura, R. D. S. G. Campilho, J. P. M. Goncalves, Pure mode II fracture  
3 characterization of composite bonded joints, *International Journal of Solids and Structures*  
4 46 (6) (2009) 1589–1595. doi:10.1016/j.ijsolstr.2008.12.001.  
5 URL <http://dx.doi.org/10.1016/j.ijsolstr.2008.12.001>
- 6 [40] F. Ducept, P. Davies, D. Gamby, Mixed mode failure criteria for a glass/epoxy composite  
7 and an adhesively bonded composite/composite joint, *International Journal of Adhesion and*  
8 *Adhesives* 20 (3) (2000) 233–244. doi:10.1016/S0143-7496(99)00048-2.
- 9 [41] G. Fernlund, J. K. Spelt, Mixed-mode fracture characterization of adhesive joints, *Composites*  
10 *Science and Technology* 50 (4) (1994) 441–449. doi:10.1016/0266-3538(94)90052-3.
- 11 [42] R. A. Gledhill, A. J. Kinloch, S. Yamini, R. J. Young, Relationship between mechanical prop-  
12 erties of and crack progogation in epoxy resin adhesives, *Polymer* 19 (5) (1978) 574–582.  
13 doi:10.1016/0032-3861(78)90285-9.
- 14 [43] A. J. Kinloch, S. J. Shaw, The Fracture Resistance of a Toughened Epoxy Adhesive, *The*  
15 *Journal of Adhesion* 12 (1) (1981) 59–77. doi:10.1080/00218468108071189.
- 16 [44] M. F. Kanninen, C. H. Popelar, *Advanced Fracture Mechanics*, Oxford Science Publication,  
17 New York, 1985.
- 18 [45] W. Ding, *Delamination Analysis of Composite Laminates*, Ph.D. thesis, University of Toronto  
19 (1999).
- 20 [46] Y. Wang, J. G. Williams, Corrections for mode II fracture toughness specimens of compos-  
21 ites materials, *Composites Science and Technology* 43 (3) (1992) 251–256. doi:10.1016/  
22 0266-3538(92)90096-L.
- 23 [47] M. K. Budzik, J. Jumel, N. Ben Salem, M. E. Shanahan, Instrumented end notched flexure -  
24 Crack propagation and process zone monitoring Part II: Data reduction and experimental, *In-*  
25 *ternational Journal of Solids and Structures* 50 (2) (2013) 310–319. doi:10.1016/j.ijsolstr.  
26 2012.08.030.  
27 URL <http://dx.doi.org/10.1016/j.ijsolstr.2012.08.030>
- 28 [48] N. Ben Salem, J. Jumel, M. K. Budzik, M. E. Shanahan, F. Lavelle, Analytical and experi-  
1 mental investigations of crack propagation in adhesively bonded joints with the Mixed Mode

- 2 Bending (MMB) test Part I: Macroscopic analysis & Digital Image Correlation measurements,  
3 Theoretical and Applied Fracture Mechanics 74 (1) (2014) 209–221. doi:10.1016/j.tafmec.  
4 2014.05.006.  
5 URL <http://dx.doi.org/10.1016/j.tafmec.2014.05.006>
- 6 [49] H. Cui, Delamination and Debonding Failure of Laminated Composite T-joints, Ph.D. thesis,  
7 TU Delft (2014). doi:10.4233/uuid:fcf6a51a-1abd-4751-8ae5-338dbb23bce2.
- 8 [50] S. Marzi, A. Biel, U. Stigh, On experimental methods to investigate the effect of layer thickness  
9 on the fracture behavior of adhesively bonded joints, International Journal of Adhesion and  
10 Adhesives 31 (8) (2011) 840–850. doi:10.1016/j.ijadhadh.2011.08.004.
- 11 [51] D. Alvarez Feito, Fracture Mechanics of Carbon Fibre Reinforced Plastics to Ti-alloy Adhesive  
12 Joints, Ph.D. thesis, Imperial College London (2012).
- 13 [52] F. Delvare, J. L. Hanus, P. Bailly, A non-equilibrium approach to processing Hopkinson Bar  
14 bending test data: Application to quasi-brittle materials, International Journal of Impact  
15 Engineering 37 (12) (2010) 1170–1179. doi:10.1016/j.ijimpeng.2010.07.001.  
675 URL <http://dx.doi.org/10.1016/j.ijimpeng.2010.07.001>

a) Graphical illustration for mathematical relationships



b) Specimen geometries

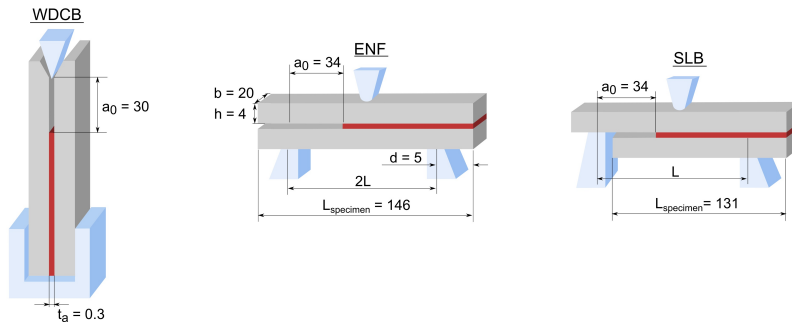


Figure 1: (a) Graphical illustration of the used orientation and nomenclature used to derive the mathematical relationships and (b) the WDCB, ENF and SLB adhesive joint fracture specimens.

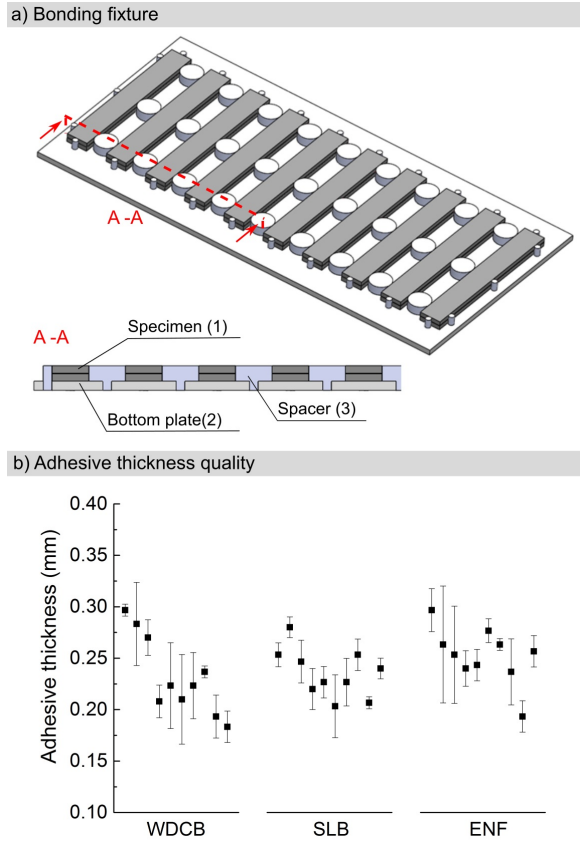


Figure 2: a) The bonding fixture used to manufacture the test specimens and b) the bondline thickness values obtained for the different test specimens. (Nominal values was 0.25 mm)

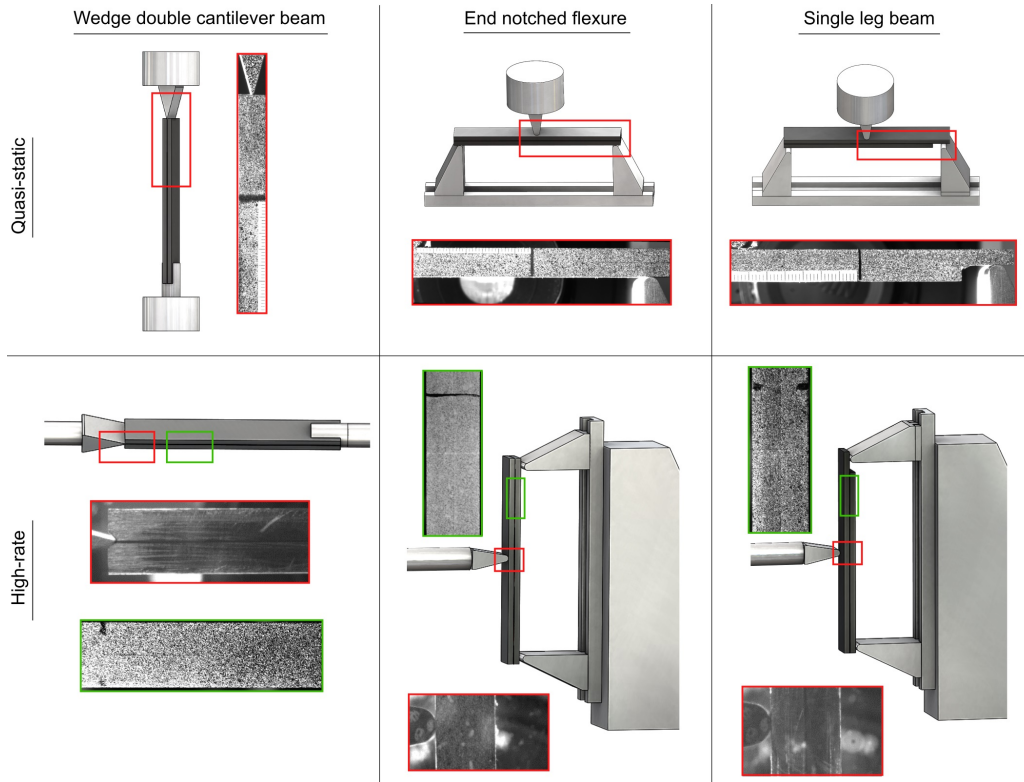
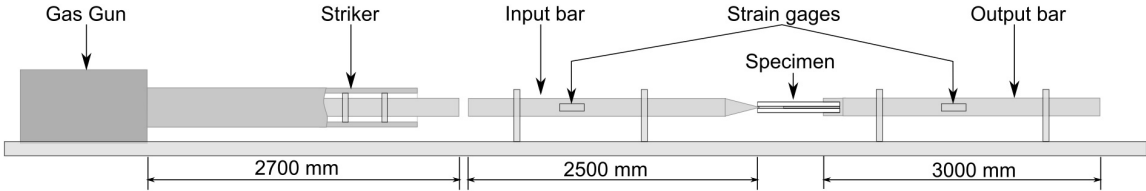


Figure 3: Quasi-static and high-rate experimental setups for the three different fracture specimens WDCB, ENF and SLB.

(a) SHPB setup for WDCB



(b) SHPB setup for ENF and SLB

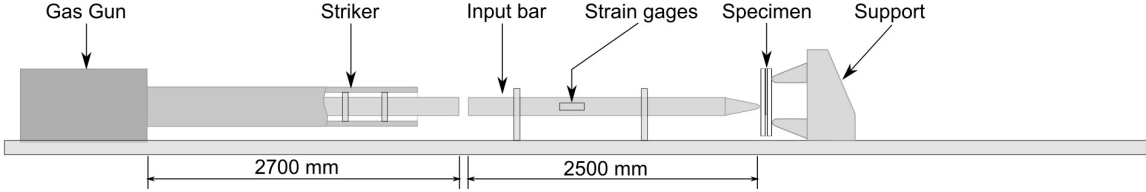


Figure 4: Schematics of the SHPB setup for (a) WDCB specimens and (b) ENF and SLB specimens.

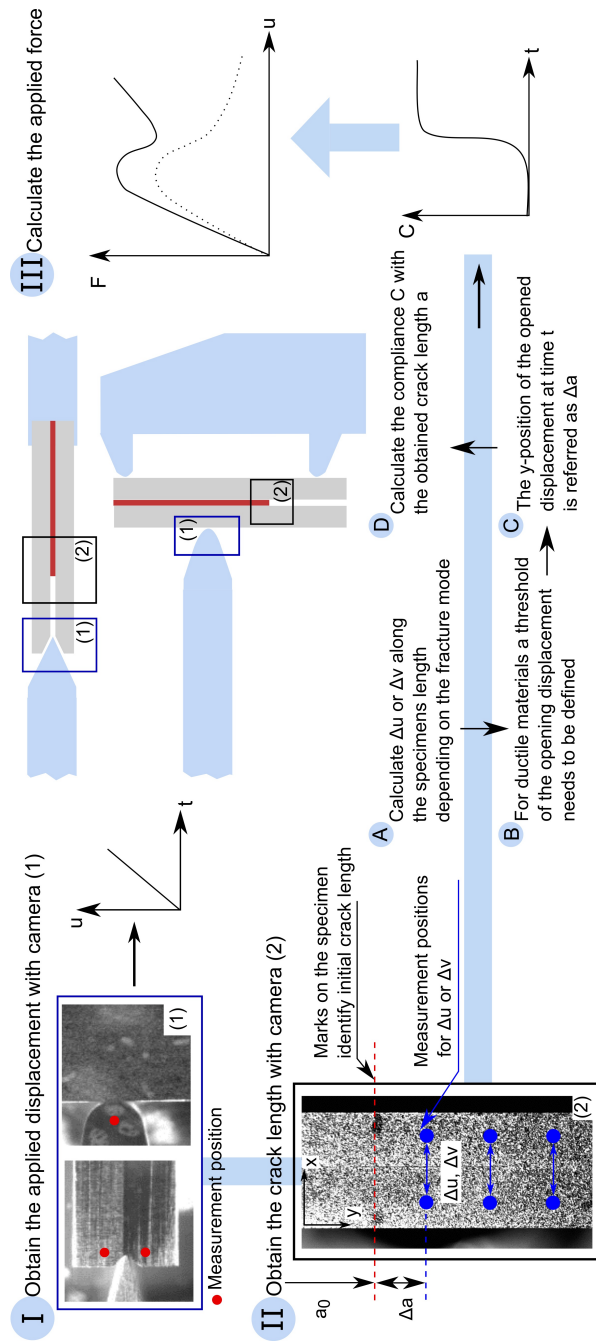


Figure 5: The strategy shows the calculation of the force-displacement curve using a new measurement technique relying entirely on DIC.

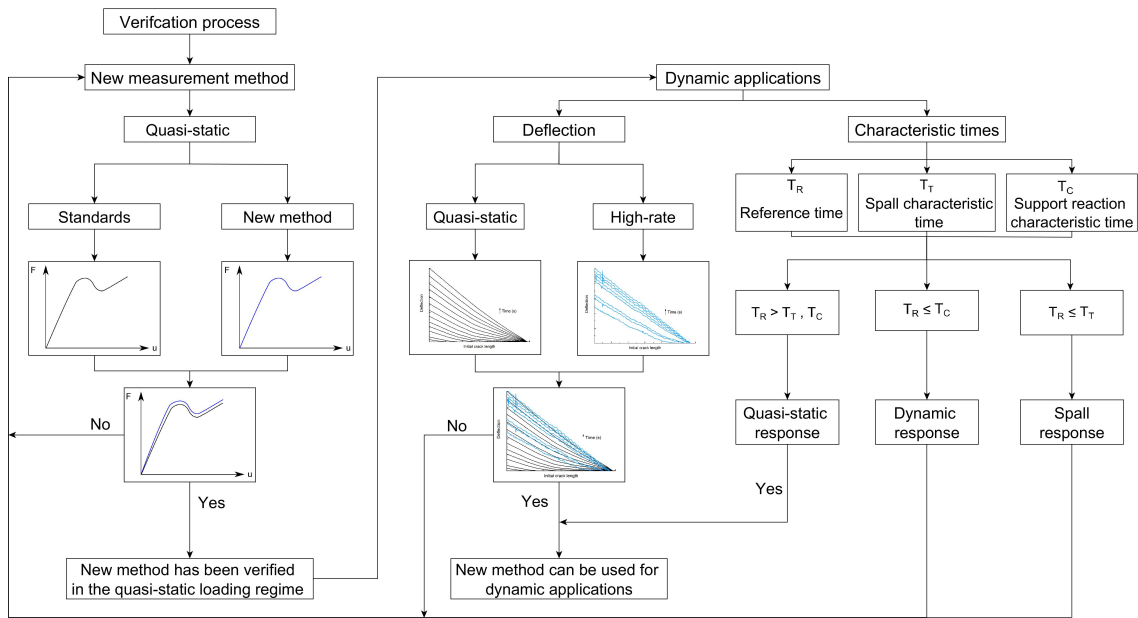


Figure 6: The new measurement technique is verified for the quasi-static and dynamic loading regime following this verification process.



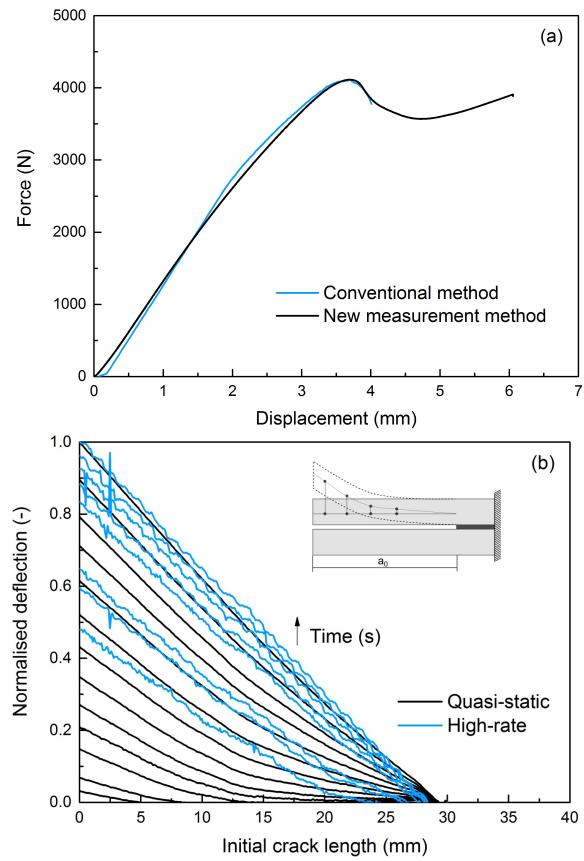


Figure 7: The new measurement technique is verified by a) the comparison of experimental ENF results calculated using standard and new method and b) the quasi-static and high-rate deflection results of a WDCB specimen.

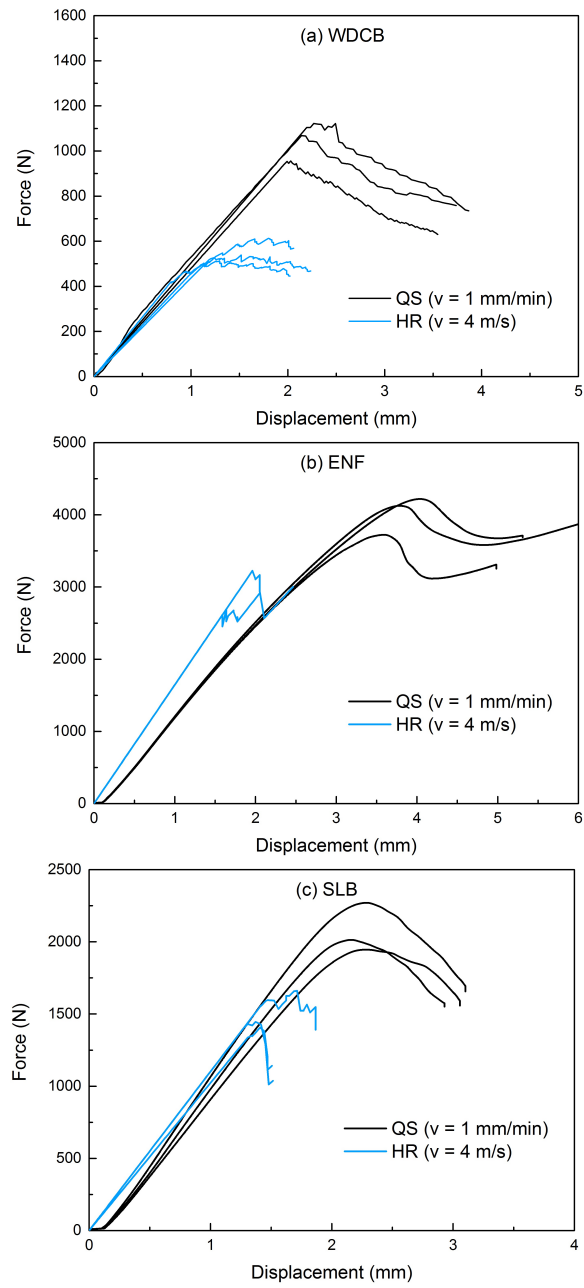


Figure 8: Rate-dependent force-displacement results for the three investigated fracture modes: a) WDCB, b) ENF and c) SLB.

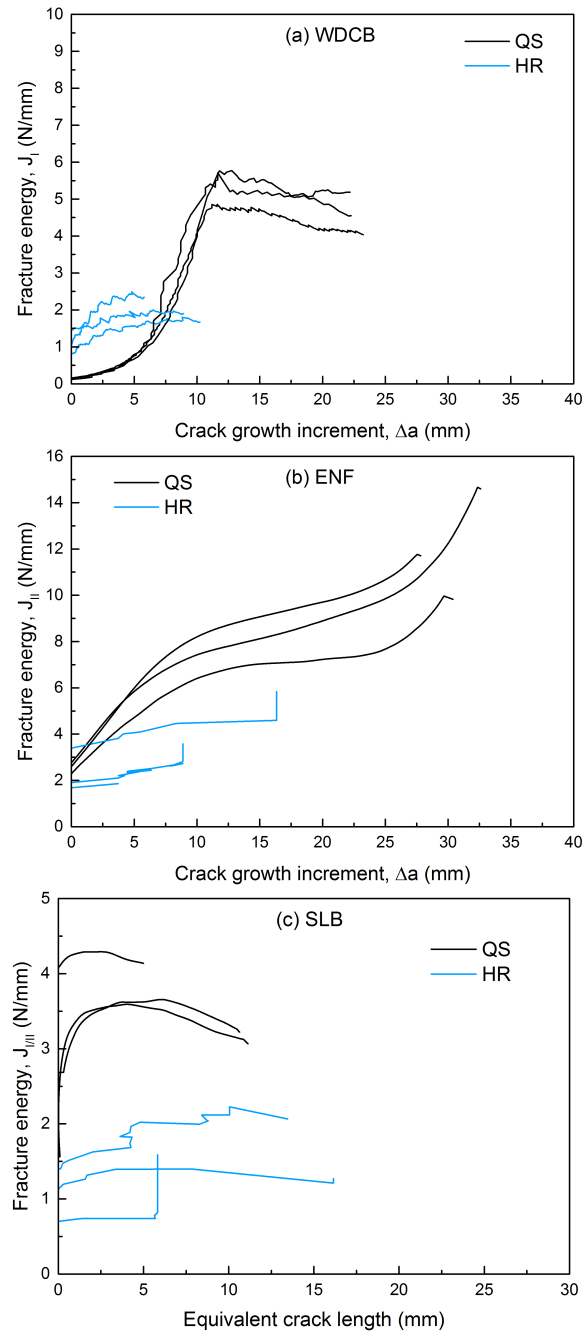


Figure 9: Rate-dependent fracture energy-crack length results for the three investigated fracture modes: a) WDCB, b) ENF and c) SLB.

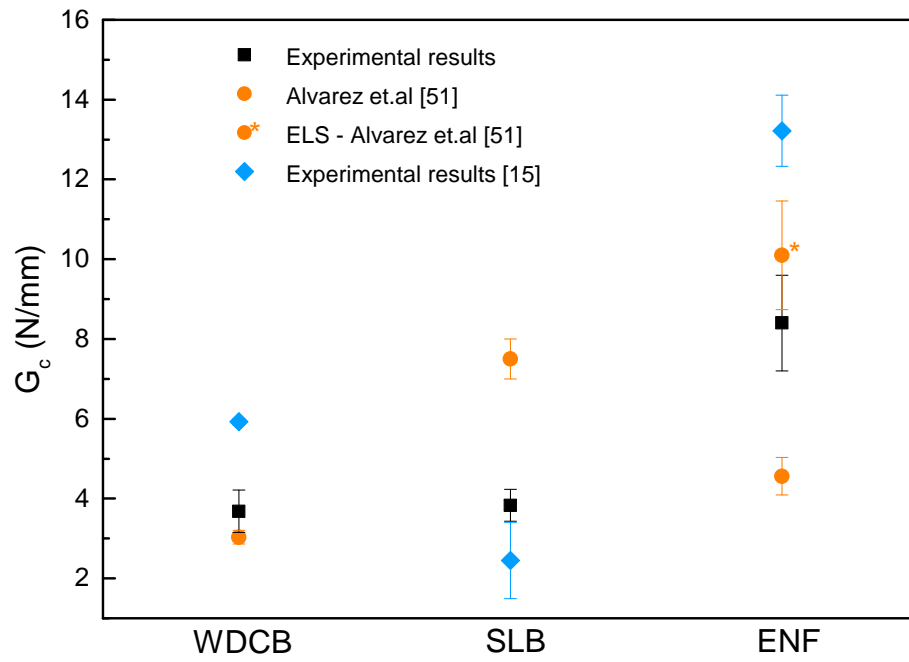


Figure 10: Fracture energy (dissipated energy) comparison between results obtained in the present study and results found in the literature.

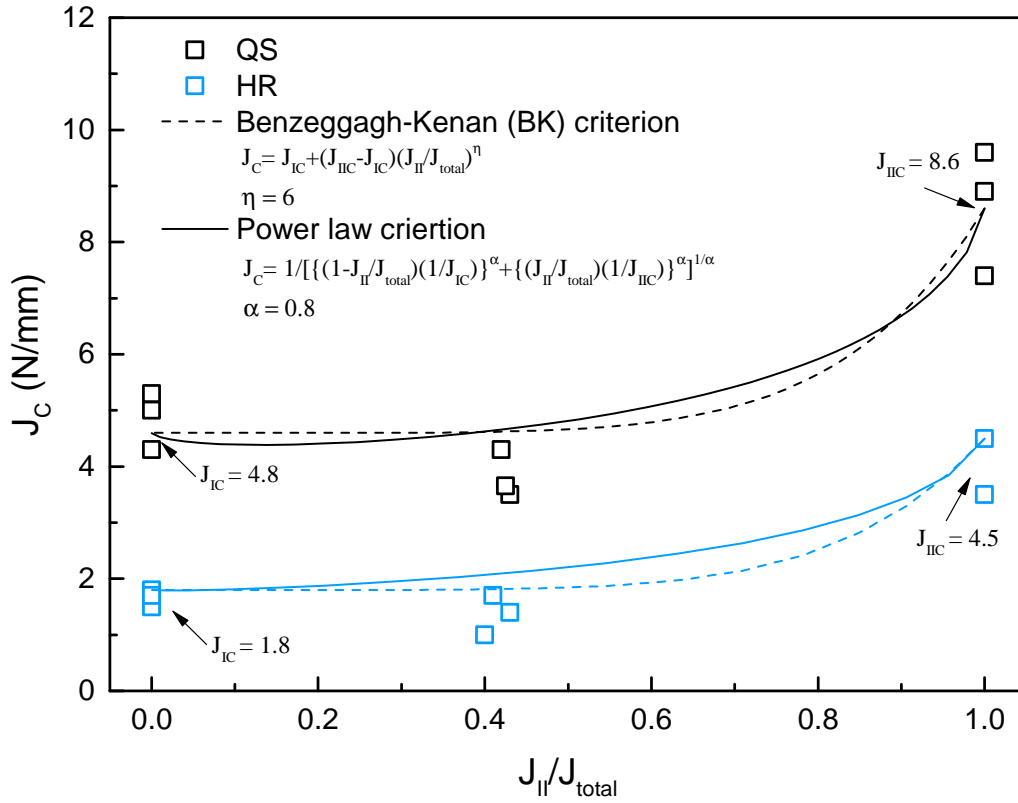


Figure 11: The failure envelope of the AF 163-2OST adhesive interface using rate-dependent experiments of WDCB (mode I), ENF (mode II) and SLB (Mixed-mode).

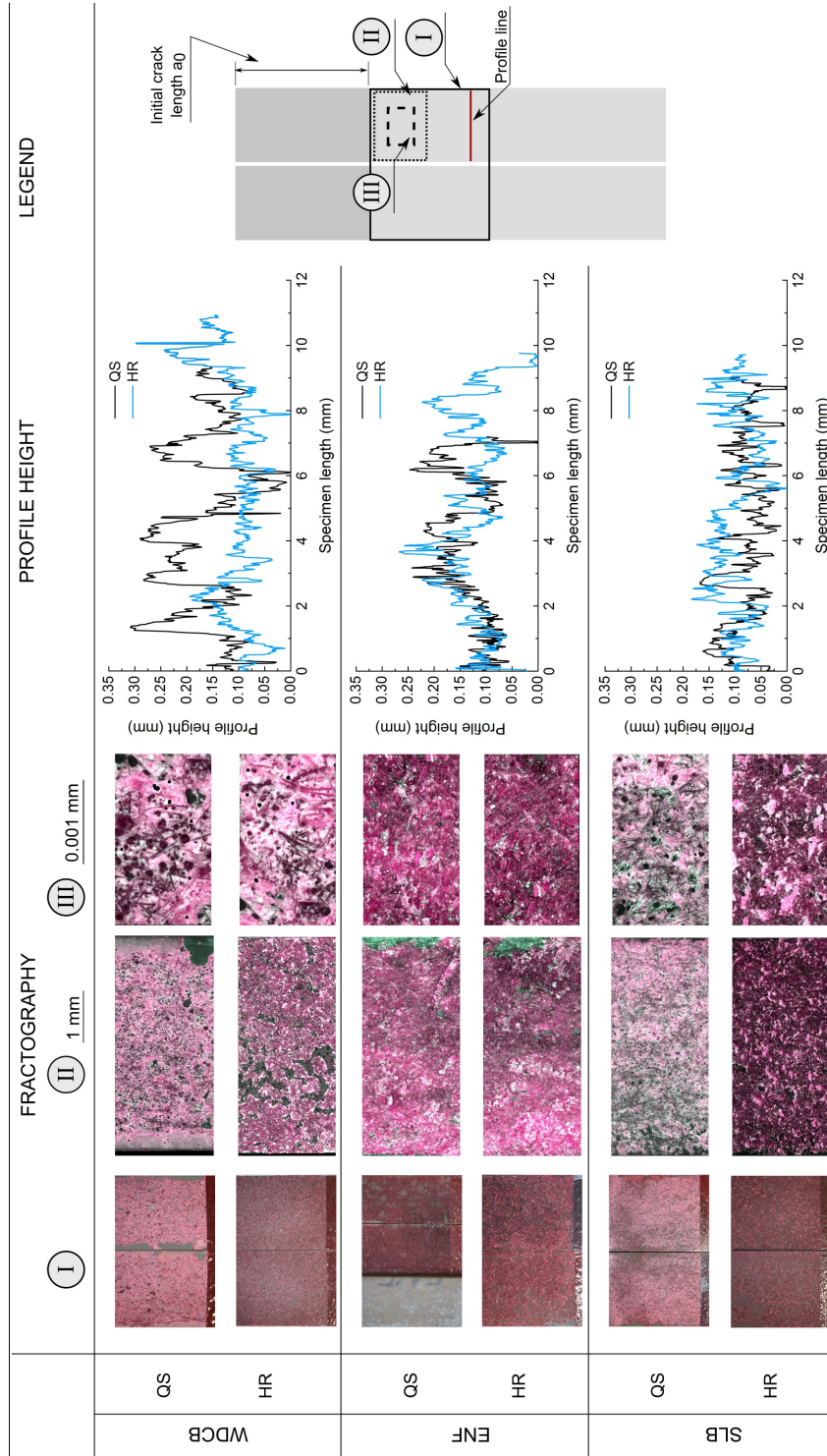


Figure 12: Fractography of representative fracture surface for WDCB, ENF and SLB specimens investigated in quasi-static and high-rate loading conditions demonstrate cohesive failure of the specimens.

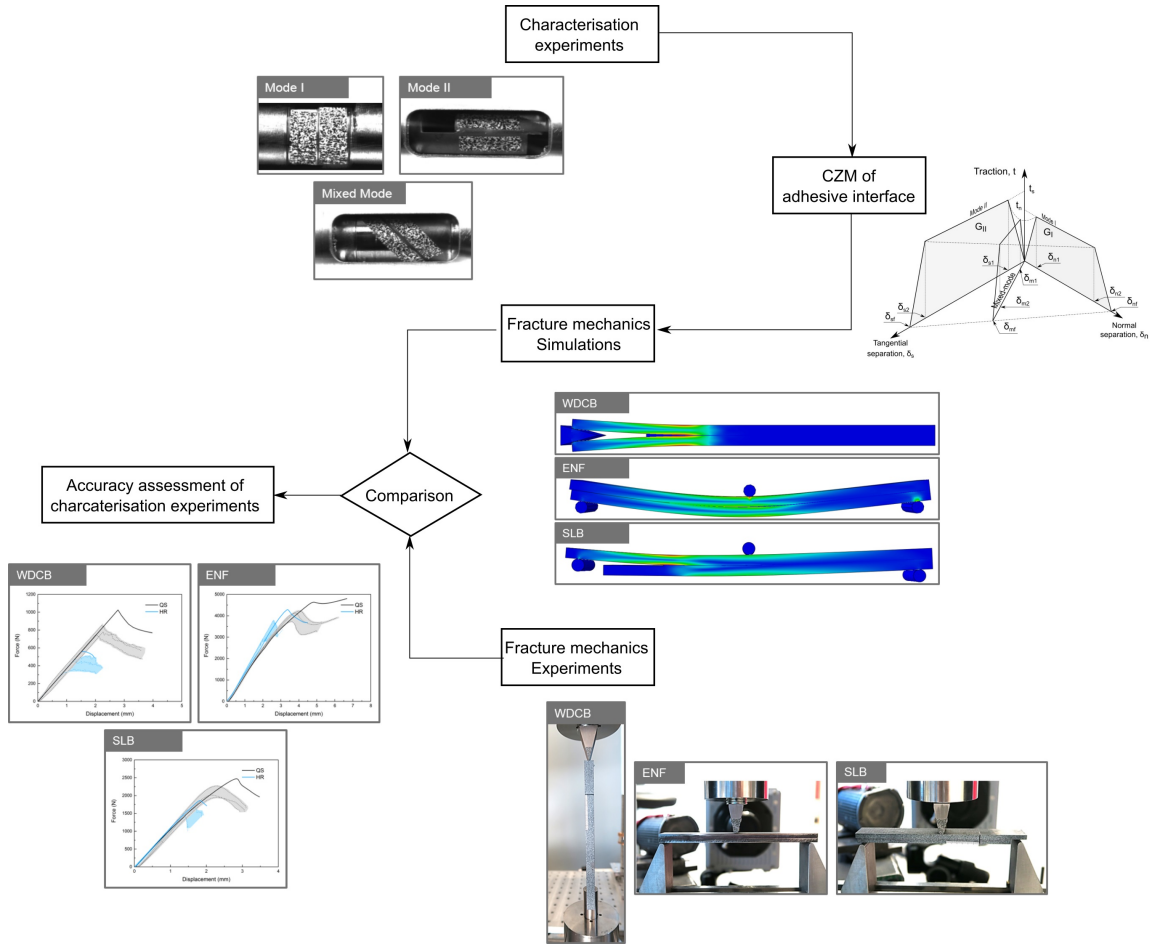


Figure 13: Process for the accuracy assessment of the developed CZM.

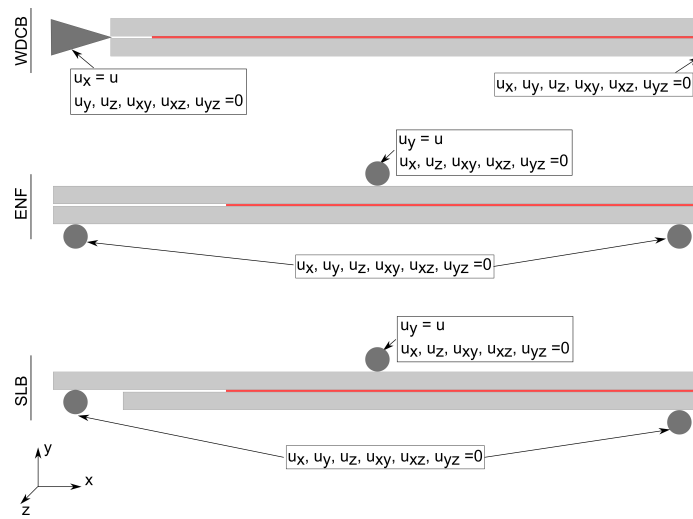


Figure 14: The simulations for the WDCB, ENF and SLB experiments are constraint with the shown boundary conditions.



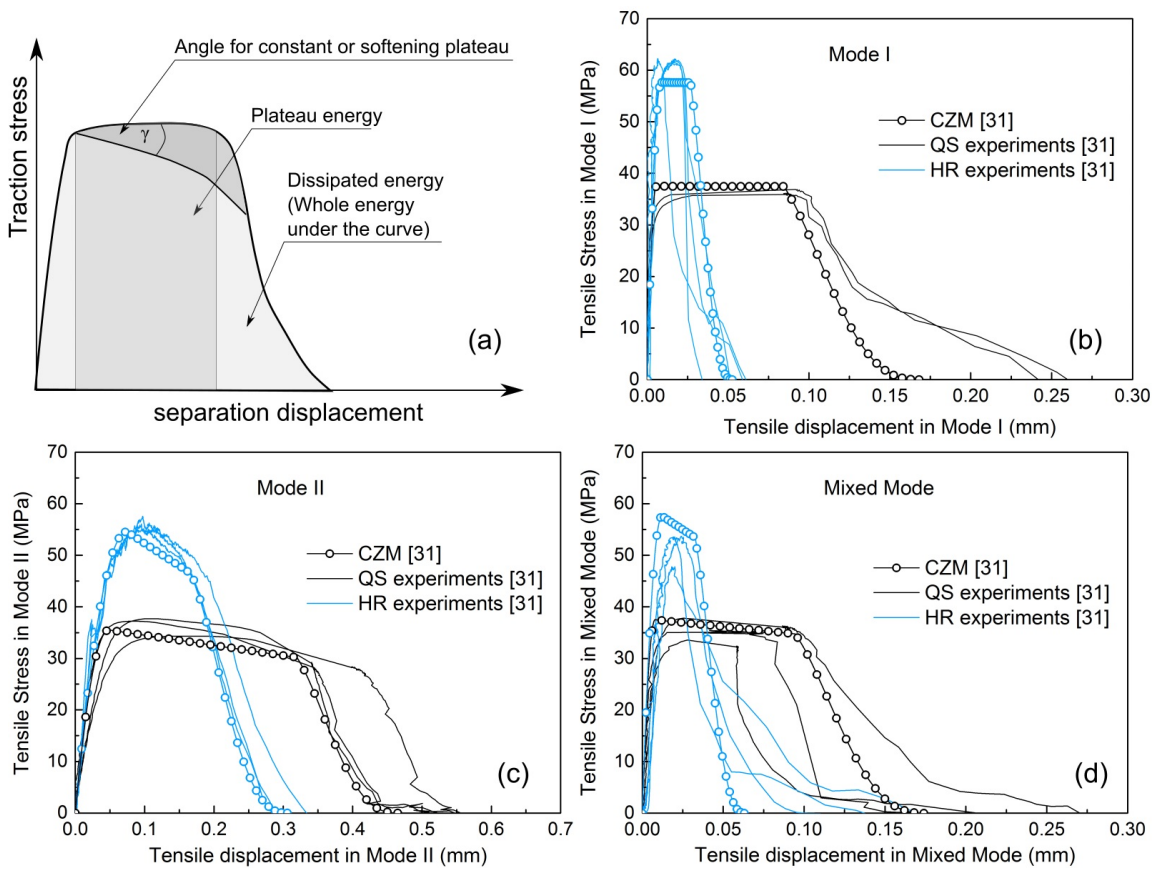
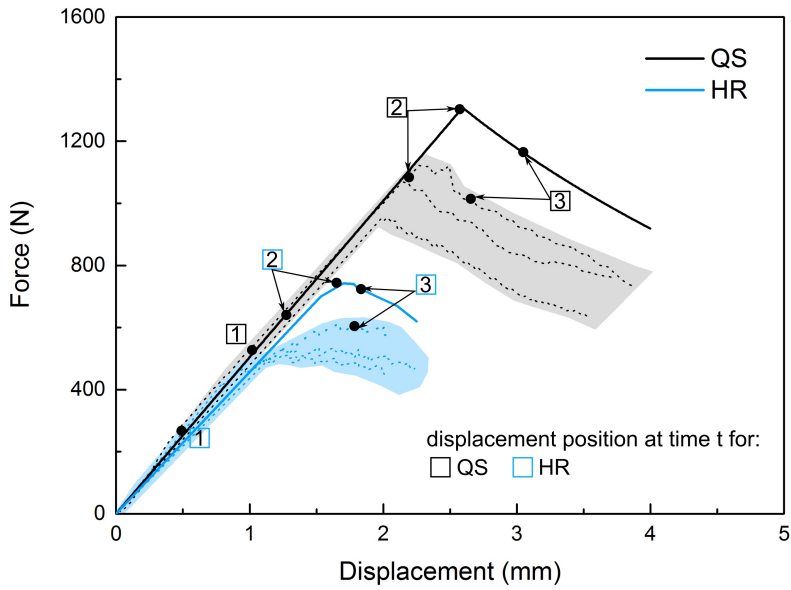


Figure 15: Representation of (a) the used terminology, (b) TSL for Mode I, (c) TSL for Mode II and (d) TSL for Mixed Mode.



Displacement field comparison of experiment and simulation at different times t:

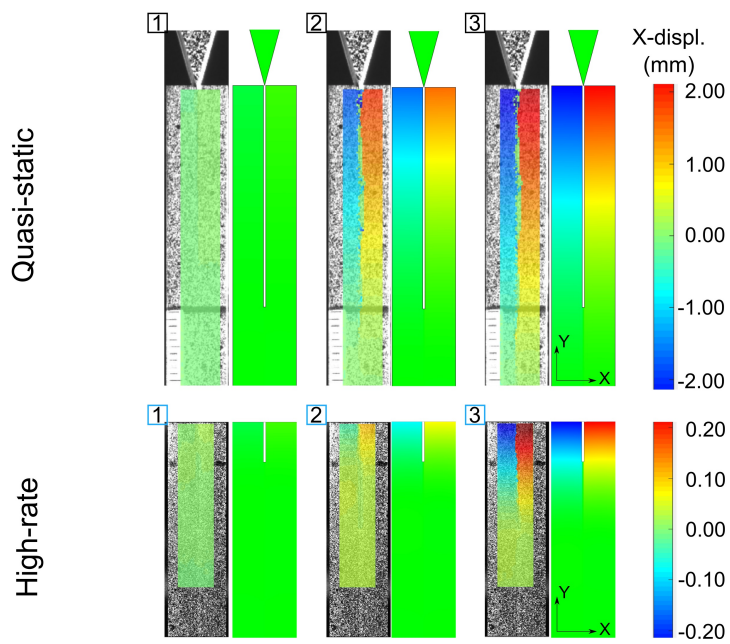
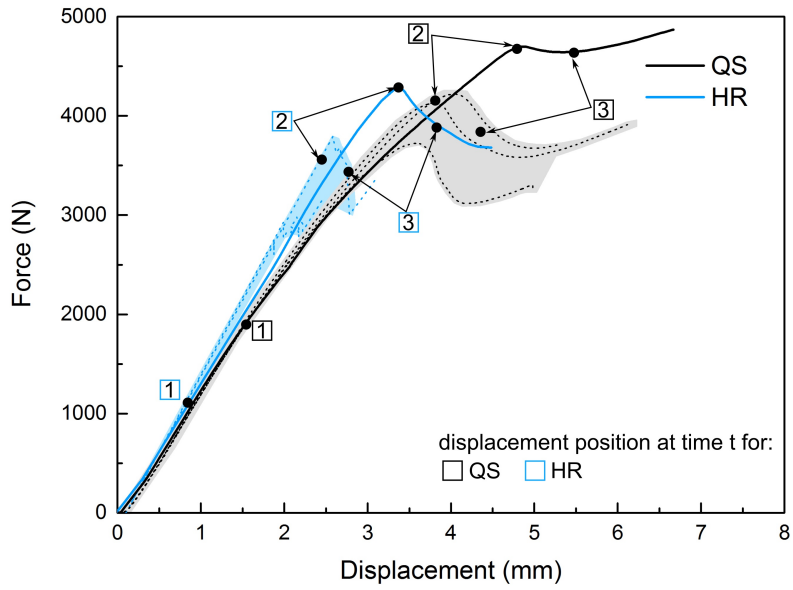


Figure 16: Comparison of rate-dependent WDCB experimented and simulated force-displacement results. Different force-displacement positions in numerical model and experiments demonstrate a good representation of the experiments using the simulations.



Displacement field comparison of experiment and simulation at different times t:

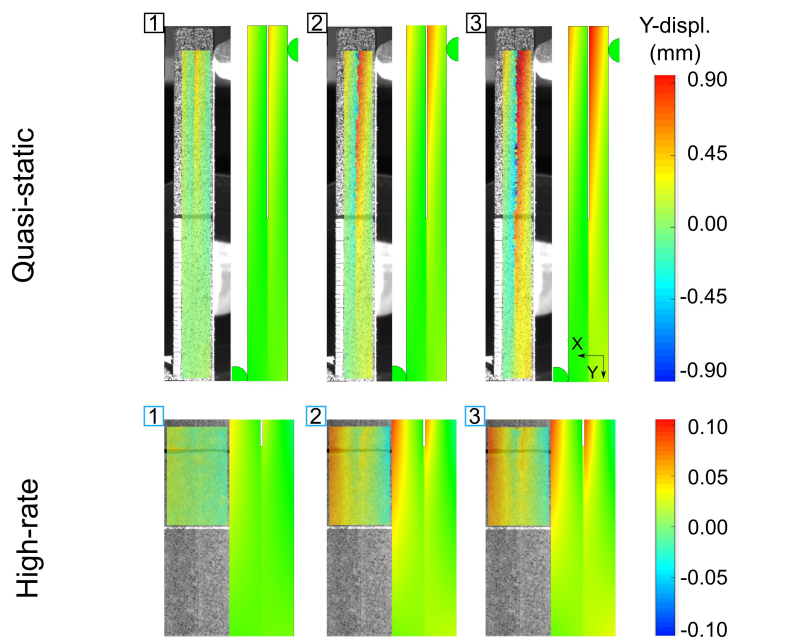
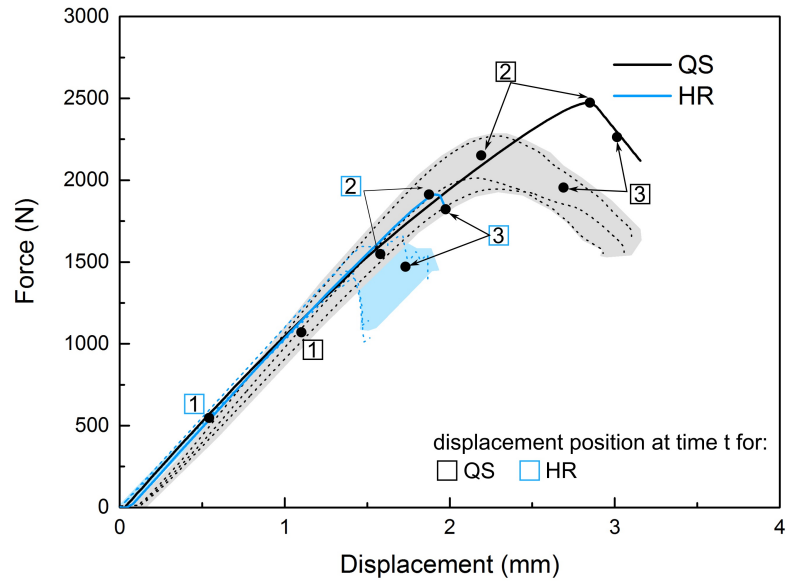


Figure 17: Comparison of rate-dependent ENF experimented and simulated force-displacement results. Different force-displacement positions in numerical model and experiments demonstrate a good representation of the experiments using the simulations.



Displacement field comparison of experiment and simulation at different times t:

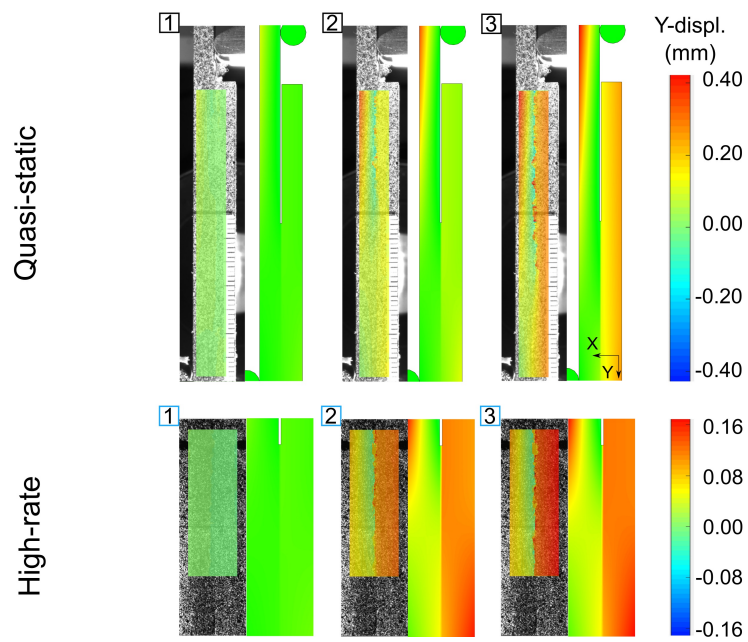


Figure 18: Comparison of rate-dependent SLB experimented and simulated force-displacement results. Different force-displacement positions in numerical model and experiments demonstrate a good representation of the experiments using the simulations.

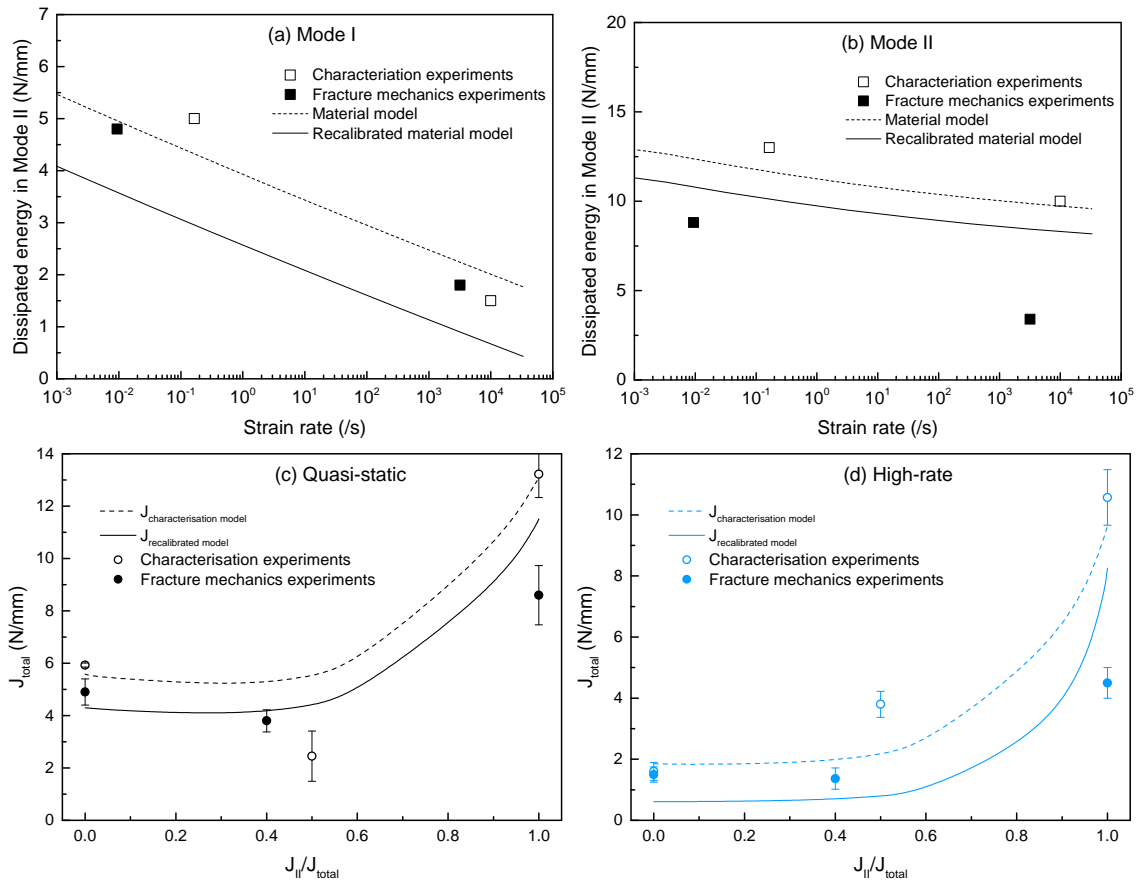


Figure 19: Comparison of the absolute values of fracture energy for characterisation [15] and validation experiments and the material model for (a) mode I and (b) mode II loading and presentation of the recalibrated material model representation compared to the material model for (c) quasi-static and (d) high-rate.

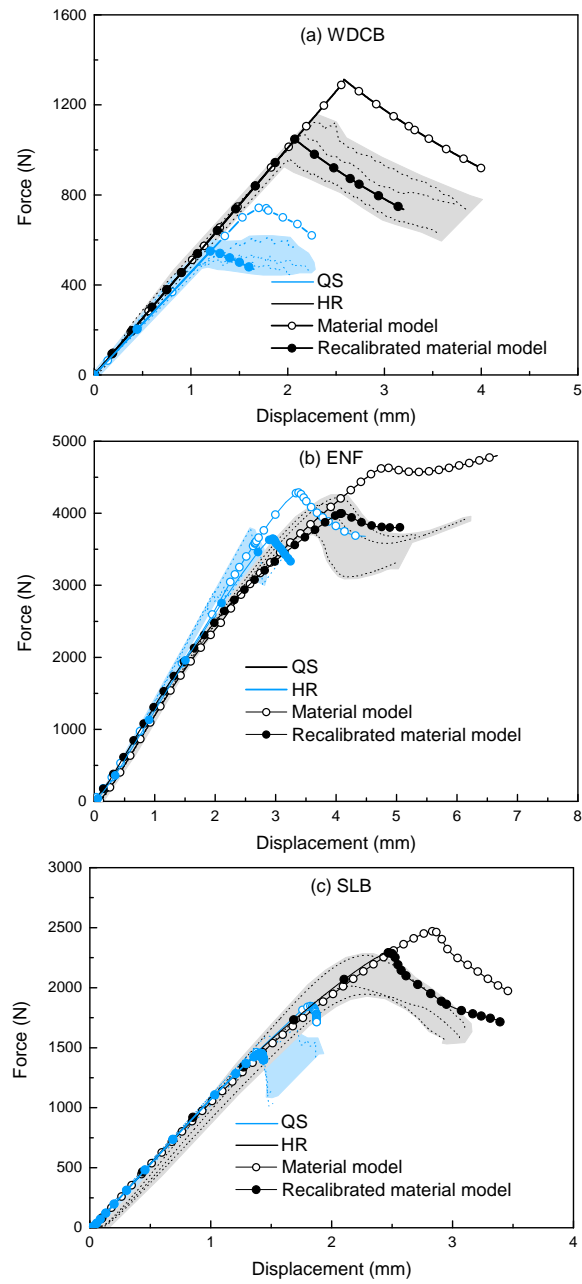


Figure 20: Representation of the corrected model to predict the experimentally obtained force-displacement curves for a) WDCB, b) ENF and c) SLB specimens.